CO2 hydrogenation to methanol over Zr- and Ce-doped indium oxide

Original
CO2 hydrogenation to methanol over Zr- and Ce-doped indium oxide / Salomone, F.; Sartoretti, E.; Ballauri, S.; Castellino, M.; Novara, C.; Giorgis, F.; Pirone, R.; Bensaid, S.. - In: CATALYSIS TODAY. - ISSN 0920-5861. - 423:(2023). [10.1016/j.cattod.2023.01.030]

Publisher:
Elsevier

Published
DOI:10.1016/j.cattod.2023.01.030

CO_2 hydrogenation to methanol over Zr- and Ce-doped indium oxide

Fabio Salomone[a,*], Enrico Sartoretti[a], Sabrina Ballauri[a], Micaela Castellino[a], Chiara Novara[a], Fabrizio Giorgis[a], Raffaele Pirone[a] and Samir Bensaid[a]

[a] *Department of Applied Science and Technology (DISAT), Polytechnic of Turin, Corso Duca degli Abruzzi 24, 10129 Turin, Italy.*

* *Corresponding author. E-mail address:* fabio.salomone@polito.it

Abstract

In recent decades, climate change has become a major issue that needs to be addressed. Many efforts have been made on the reduction of CO_2 emissions and its conversion in energy carriers and high value-added products such as methane, methanol, dimethyl-ether, and hydrocarbons. The present study focuses on the development of catalysts for hydrogenating CO_2 to methanol, which is a useful chemical and an alternative liquid fuel. According to the literature, In_2O_3-based catalysts are particularly selective in the hydrogenation of CO_2 to methanol, reducing the production of CO even at high space velocities compared to the more common ternary catalysts such as $Cu/ZnO/Al_2O_3$ or $Cu/ZnO/ZrO_2$. Therefore, the effects of CeO_2 and ZrO_2 on In_2O_3-based catalysts were investigated in the present study. The In_xCe_{100-x} and the In_xZr_{100-x} mixed oxides catalysts were synthesized via gel-oxalate coprecipitation by varying the atomic ratios between the elements. Subsequently, they were analysed with several characterisation techniques to rationalise the catalytic performances that were obtained by testing the samples in a fixed bed reactor under different reaction conditions. The addition of different amounts Ce or Zr modified the structure and morphology of the samples and promoted the adsorption of CO_2 from 1.8 $mmol_{CO2}\cdot g_{cat}^{-1}$ up to 10.6 $mmol_{CO2}\cdot g_{cat}^{-1}$. ZrO_2 stabilises the structure and the results suggests that the greater specific activity (168 $mg_{CH3OH}\cdot g_{In2O3}^{-1}\cdot h^{-1}$ at 300 °C and 2.5 MPa of $In_{40}Zr_{60}$) could be ascribed to the electronic promotion of Zr. On the contrary, the addition of CeO_2 did not reveal a beneficial effect on the activity. Concerning the stability, In_2O_3-ZrO_2 binary oxides seemed to be affected mainly by sintering; whereas In_2O_3-CeO_2 were affected by at least three deactivating phenomena: sintering, reduction of In_2O_3 to metallic indium and coking. Consequently, the deactivation rate of these binary oxides increased from $1.04 \cdot 10^{-2}$ h^{-1} of the In_{100} to $4.13 \cdot 10^{-2}$ h^{-1} of the $In_{40}Ce_{60}$.

Keywords

Indium oxide, ceria, zirconia, methanol, CO_2 hydrogenation

Highlights

- CeO_2 and ZrO_2 modify the morphology and boost the CO_2 adsorption rate.
- The electronic promotion effect of Zr enhances the methanol synthesis from CO_2.
- ZrO_2 stabilises the structure and mitigates the deactivation phenomena.
- CeO_2 increases the reducibility of the samples without stabilising the structure.
- In_2O_3-CeO_2 samples are affected by sintering, formation of metallic In and coking.

1 Introduction

In recent years, greenhouse gas emissions have become a serious problem due to the progressive increase in the global average temperature. Therefore, the mitigation of the climate change and the reduction of CO_2 emissions are crucial challenges to be faced. Consequently, energy production technologies are progressively changing and, in particular, renewable energy sources, such as wind or photovoltaic, are progressively replacing non-renewable fossil energy sources. However, fossil fuels are still widely used in many industrial fields and in the transport sector, where their full replacement is tricky. The goal of the society is the achievement of the closed carbon cycle by producing alternative fuels from CO_2, which can be captured from flue gases or from the environment. Power-to-Fuels and Emission-to-Fuels processes aim to exploit the electricity generated from renewable energy sources to produce an energy carrier such as H_2 [1–4], which can be exploited in CO_2 hydrogenation processes to obtain alternative fuels or sustainable value-added chemicals (e.g. methane, methanol, dimethyl-ether, liquid hydrocarbons, light olefins, etc.) [5–14].

Methanol is one of the most important components in the chemical industry, as it is widely used as a solvent and chemical agent for the synthesis of other products [15–17]. The CO_2 hydrogenation to methanol is an exothermic reaction and it is thermodynamically unfavoured by the temperature increase; instead, the reverse water gas shift reaction is endothermic and thermodynamically favoured at higher temperatures. The overall process involves three main reactions: the CO_2 and the CO hydrogenation to methanol and the reverse water gas shift, as reported in equations (1), (2) and (3), respectively.

$$CO_{2(g)} + 3H_{2(g)} \rightleftarrows CH_3OH_{(g)} + H_2O_{(g)} \qquad \Delta\widetilde{H}^0_{298.15} = -\,49.4\ \text{kJ/mol} \tag{1}$$

$$CO_{(g)} + 2H_{2(g)} \rightleftarrows CH_3OH_{(g)} \qquad \Delta\widetilde{H}^0_{298.15} = -\,90.4\ \text{kJ/mol} \tag{2}$$

$$CO_{2(g)} + H_{2(g)} \rightleftarrows CO_{(g)} + H_2O_{(g)} \qquad \Delta\widetilde{H}^0_{298.15} = +\,41.2\ \text{kJ/mol} \tag{3}$$

The CO_2 hydrogenation process is extensively studied in the literature and many articles support its technical and economic feasibility for industrial scale production [5,8,16,18–21]. Cu-based catalysts (i.e. $Cu/ZnO/Al_2O_3$ or $Cu/ZnO/ZrO_2$) are the most studied for this application [17,22–24]. However, some researchers have lent particular attention to In_2O_3-based catalysts [13,25,26].

More specifically, Martin *et al.* [26] have demonstrated the superior efficiency in CO_2 hydrogenation to methanol of In_2O_3-based catalysts, achieving 100% methanol selectivity under industrial relevant reaction conditions [25,26]. They have suggested that the reaction mechanism consists in the formation and annihilation of oxygen vacancies on the surface of the catalytic material that enhance the catalytic performances and stabilises In_2O_3 [26,27]. Moreover, they have confirmed that the indium oxide deposited on a zirconia support showed excellent stability over a 1000-h endurance test under the reaction conditions [26]. Hence, according to these recent studies, In_2O_3-ZrO_2 catalysts appear to be very promising materials for sustainable methanol production. Moreover, the increase of CO_2 adsorption capacity of In_2O_3 supported on CeO_2 could be a promising aspect for the capacity of converting CO_2 into methanol [27]. Other researchers have demonstrated the beneficial effects of the addition of CeO_2 into the catalysts [28], and in the literature, it is known that the high catalytic activity of ceria is often linked to its ability to acquire and release oxygen atoms forming oxygen vacancies [29,30].

Therefore, this work aims to study the behaviour of co-precipitated In_2O_3-CeO_2 and In_2O_3-ZrO_2 binary oxide catalysts for the methanol synthesis process to reduce CO production and maximize methanol productivity. Furthermore, the goal is to rationalise the experimental evidence on both activity and stability of the samples by means of different characterisation techniques.

2 Methodology

2.1 Synthesis of the catalysts

All the catalysts were prepared by gel-oxalate co-precipitation varying the atomic ratios of metals. A 0.1 M solution of metal nitrates (i.e., $In(NO_3)_3 \cdot nH_2O$ and $Ce(NO_3)_3 \cdot 6H_2O$ or $ZrO(NO_3)_2 \cdot nH_2O$) in ethanol with the proper atomic ratio and a 1 M solution of oxalic acid in ethanol were prepared [23,24,31]. After that, the oxalic acid solution (an excess of 20 % of solution was used [32,33]) was rapidly poured (~1 $mL \cdot s^{-1}$) into the nitrate solution, which was kept at room conditions under vigorous stirring, and the gel was aged for 2 h at these conditions [32,33]. The precipitate was separated from the solvent by centrifugation and then it was dried at 60 °C overnight. Finally, the dried precipitate was calcined at 360 °C for 4 h (heating rate: 10 $°C \cdot min^{-1}$) and then ground in an agate mortar for obtaining the catalyst powder. For the sake of clarity, the binary oxide catalysts were labelled In_xCe_{100-x} and In_xZr_{100-x}, where x represents the nominal atomic percentage of indium; in this work x was set equal to 0, 40, 60, 80 and 100 at.%.

2.2 Characterization of the catalysts

Textural properties of calcined and spent catalysts were investigated by N_2 physisorption at 77 K using a Micromeritics Tristar II ASAP 3020 analyser. Each sample was previously outgassed in a Micromeritics FlowPrep 060 at 200 °C for 2 h flowing nitrogen to remove adsorbed contaminants and moisture from the surface. The specific surface area was determined according to the Brunauer-Emmett-Teller theory [34,35] and the porosimetry analysis was performed by applying the Barrett-Joyner-Halenda algorithm to the desorption branch of the isotherm [36].

The X-ray diffractograms of the powders were collected at room conditions by using a Philips X'Pert PW3040 diffractometer operating at 40 kV and 40 mA, using a Ni β-filtered Cu-Kα radiation characterized by a wavelength (λ) equal to $1.5406 \cdot 10^{-10}$ m. The XRD data were collected over the 2θ angle range of 20°– 80°, with a scan step size of 0.013° 2θ and a time per step equal to 0.3 s, while the average crystallite size of each phase was calculated according to Scherrer's equation [37] and the lattice strain was evaluated by using the Williamson-Hall's equation [38,39].

The catalysts were observed with a field emission scanning electron microscope (FE-SEM) Zeiss Merlin equipped with a Gemini-II column, for the purpose of analysing their morphology. Moreover, energy dispersive X-ray spectroscopy (EDS) was employed to determine the elemental composition of portions of the catalysts. In addition, the elemental composition of the catalysts was determined by using an inductively coupled plasma mass spectrometer (iCAP Q ICP-MS, Thermo Fisher Scientific). Briefly, each calcined catalyst (~100 mg) was digested in 30 mL of an acid aqueous solution (0.25 M L-ascorbic acid and 0.5 M H_2SO_4) at room temperature overnight [40]. Each solution was diluted by using deionised water to have 100 mL of concentrated solution. After that, each concentrated solution was diluted using deionised water to achieve the concentration of each element within the calibration range (i.e., 100 – 2000 ppb), then these samples were analysed by using ICP-MS.

Temperature-programmed measurements were carried out using a Thermoquest TPD/R/O 1100 analyser equipped with a thermal conductivity detector (TCD). Firstly, the reducibility properties of the samples were investigated by means of H_2-TPR. Each catalyst (~20 mg of calcined sample) was placed in a quartz tube reactor and pre-treated at 350 °C (+10 $°C \cdot min^{-1}$) for 1 h in He flow (20 $mL \cdot min^{-1}$) to simulate the pre-treatment prior to the catalytic tests. After that the sample was cooled to 40 °C and the H_2-TPR measurement was performed by using a constant flowrate of 20 $mL \cdot min^{-1}$ of 5.00 vol.% H_2/Ar and by heating the oven from 40 °C to 900 °C (+10 $°C \cdot min^{-1}$). Furthermore, the affinity of the CO_2 with the surface of the spent catalysts was investigated by means of CO_2-TPD measurements. To perform the analysis, a mass of approximately 100 mg was placed in the quartz tube reactor between two layers of quartz wool and cleaned with He (20 $mL \cdot min^{-1}$) at

300 °C (+10 °C·min^{-1}) for 1 h. Subsequently, the sample was cooled down to 40 °C in He and immediately after it was saturated using pure CO_2 (20 mL·min^{-1}) at 40 °C for 1 h. Once the catalyst was saturated, it was cleaned with He (20 mL·min^{-1}) at 40 °C for 1 h. Finally, the CO_2-TPD was performed by flowing 20 mL·min^{-1} of He and heating the sample from 40 °C to 900 °C (+10 °C·min^{-1}).

The amount of carbonaceous compounds on the surface of the spent catalysts was estimated using temperature-programmed combustion (TPC) analyses. Each sample (~50 mg) was placed in a U-shaped quartz tube and the measurement was performed by flowing 100 NmL·min^{-1} of 5 vol.% O_2/N_2 from room temperature to 750 °C (heating rate: +10 °C·min^{-1}). The gas at the outlet of the reactor was analysed by means of an ABB Uras 14 gas analyser to measure the concentration of CO and CO_2.

The surface of the catalysts was investigated via X-ray photoelectron spectroscopy (XPS) employing a PHI 5000 Versa Probe equipment, using, for survey scans, a band-pass energy of 187.85 eV, a take-off angle of 45° and an X-ray spot diameter of 100 μm; high resolution (HR) spectra were collected using a band-pass energy of 23.50 eV.

Raman analyses of the In_xCe_{100-x} catalysts were carried out using a Renishaw InVia Reflex micro-Raman spectrometer to study the defectiveness of the materials. The instrument is equipped with a 100 mW solid-state laser emitting monochromatic light (wavelength: 514.5 nm). The Raman spectra were collected under a 5x objective with a total acquisition time of 225 s. The results were elaborated with the Renishaw software WiRE 3.4. The D/F_{2g} ratio was calculated as previously described [41], by fitting the defect band with three Lorentzian peaks located around 560, 590 and 620 cm^{-1}. An additional Lorentzian peak centred at 625 cm^{-1} was introduced to consider a typical feature of In_2O_3 in this position; the area of the latter component, which does not contribute to the D band area, was set proportional to the main In_2O_3 peak at 308 cm^{-1}. It is worth noting that In_xZr_{100-x} samples could not be analysed due to excessive fluorescence.

The Fourier-transform infrared (FT-IR) analyses of the In_xZr_{100-x} samples were performed by means of a Bruker Invenio S spectrophotometer equipped with a Mercury-Cadmium-Telluride (MCT) IR detector. Each sample was mixed with KBr in a mass ratio of 1:4 to obtain a homogeneous powder. After that, some powder was pelletised at 44 kN by producing a small thin tablet with an apparent density of 20 mg·cm^{-2}. The IR spectra were always collected at room temperature between 4000 cm^{-1} and 400 cm^{-1} with a resolution of 2 cm^{-1}. Prior to the measurements, each sample was outgassed at 0.01 Pa for 30 min at room temperature or at 100 °C, 200 °C or 300 °C.

2.3 Catalytic tests

The catalytic activity of each sample was investigated in a fixed-bed stainless steel reactor (catalyst load: 1.0 g). The catalytic bed had an annular section (i.d. 3 mm, o.d. 8 mm) due to the presence of an innertube, in which a thermocouple was inserted for the measurement of the reaction temperature within the catalytic bed.

Concerning the catalytic tests, each sample was pre-treated in situ at 350 °C for 1 h by using pure nitrogen (30 $NL \cdot h^{-1}$) at 0.2 MPa. Subsequently, each sample was tested continuatively (stability test) for 20 h at 275 °C, 2.5 MPa and 20 $NL \cdot g_{cat}^{-1} \cdot h^{-1}$ (inlet composition: 60 vol.% H_2, 20 vol.% CO_2 and 20 vol.% N_2). After the stabilization, activity tests were performed on each catalyst at 2.5 MPa, 20 $NL \cdot g_{cat}^{-1} \cdot h^{-1}$ (inlet composition: 60 vol.% H_2, 20 vol.% CO_2 and 20 vol.% N_2) varying the reaction temperature between 200 °C and 300 °C. At the end of the catalytic tests, the catalyst was removed from the reactor, sieved to remove quartz wool fibres and collected to characterise it.

The gases at the outlet of the reactor were split in two streams. On the one side, a portion of the gases was directly analysed by using a gas chromatograph (7890B GC System, Agilent Technologies) equipped with a heated transfer line (120 °C, atmospheric pressure), a two-columns separation system (HP-PLOT/Q and HP-PLOT Molesieve) connected to a thermal conductivity detector (TCD) and a flame ionization detector (FID). On the other side, water and methanol were condensed in a small tank (room temperature and 2.5 MPa), then the gaseous stream was completely dehydrated using a silica gel trap (room temperature and atmospheric pressure), and it was eventually analysed with an in-line X-STREAM EMERSON gas analyser equipped with two nondispersive infrared (NDIR) sensors and a thermal conductivity detector (TCD) for monitoring CO, CO_2 and H_2 concentrations, respectively.

The CO_2 conversion (ζ_{CO_2}, dimensionless), the selectivity (σ_i, dimensionless) and the yield (η_i, dimensionless) of a generic i-th product were evaluated by means of equations (4), (5) and (6), respectively. For the sake of clarity, $\dot{n}_{CO_2,in}$ ($mol \cdot h^{-1}$) and $\dot{n}_{CO_2,out}$ ($mol \cdot h^{-1}$) are the inlet and outlet CO_2 molar flow rates, respectively; $N_{C,i}$

(dimensionless) is the number of carbon atoms of the i-th chemical species and $\dot{n}_{i,out}$ (mol·h^{-1}) is the outlet molar flow rate of the i-th compound. Normal conditions were assumed equal to 0 °C and 0.1 MPa.

$$\zeta_{CO_2} = \frac{\dot{n}_{CO_2,in} - \dot{n}_{CO_2,out}}{\dot{n}_{CO_2,in}} \tag{4}$$

$$\sigma_i = \frac{N_{C,i} \cdot \dot{n}_{i,out}}{\dot{n}_{CO_2,in} - \dot{n}_{CO_2,out}} \tag{5}$$

$$\eta_i = \zeta_{CO_2} \cdot \sigma_i = \frac{N_{C,i} \cdot \dot{n}_{i,out}}{\dot{n}_{CO_2,in}} \tag{6}$$

The molar fractions of CO_2, N_2, CO, CH_4, CH_3OH and CH_3OCH_3 were estimated by using calibration curves, the molar fraction of water was evaluated by means of the stoichiometry of the reactions and by taking into account the vapour pressure in the condensation tank; whilst the molar fraction of H_2 was evaluated by assuming that the sum of the molar fractions is equal to 1, because the sensitivity of the TCD detector to a variation of H_2 with respect to He (carrier) is too small due to the similar thermal conductivity of the two gases. The total outlet molar flow rate ($\dot{n}_{out}$, mol·h^{-1}) was estimated by assuming that the molar flow rate of the inert species (i.e., N_2) did not vary during the process, as reported in equation (7); where $\dot{n}_{in}$ (mol·h^{-1}) is the total inlet molar flow rate, $y_{N_2,in}$ and $y_{N_2,out}$ are respectively the inlet and outlet N_2 molar fraction.

$$\dot{n}_{out} = \dot{n}_{in} \cdot \frac{y_{N_2,out}}{y_{N_2,in}} \tag{7}$$

Lastly, the uncertainty on the calculations was propagated according to equation (8), where $f(x_1, \dots, x_n)$ is a function of n variables (x_j), Δf is the uncertainty of the result of the function $f(x_1, \dots, x_n)$ and Δx_j is the uncertainty of a generic j-th variable.

$$\Delta f(x_1, \dots, x_n) = \left[\sum_{j=1}^{n} \left(\frac{\partial f}{\partial x_j} \cdot \Delta x_j\right)^2\right]^{0.5} \tag{8}$$

2.4 *Deactivation kinetic model*

According to the literature [42], to study the deactivation phenomena, a 1st order kinetic of the reaction rate and a 1st order kinetic of the deactivation rate independent from the concentration of the reactants have been considered, as reported in the system of equations (9). In those equations, r_{CO_2} (mol$_{CO2}$·m^{-3}·h^{-1}) is the CO_2 conversion rate, k' ((mol$_{CO2}$·m^{-3})$^{1-n}$·h^{-1}) is the Arrhenius' temperature-dependent kinetic constant of the reaction rate, C_{CO_2} ($\mathrm{mol_{CO2} \cdot m^{-3}}$) is the CO_2 concentration in the gas phase, *n* (dimensionless) is the order of reaction, *a* (dimensionless) is the activity of the catalyst, *da/dt* (h^{-1}) is the deactivation rate, k_d ($(\mathrm{mol_{CO2} \cdot m^{-3}})^{1-m} \cdot h^{-1}$) is the Arrhenius' temperature-dependent constant of deactivation, *d* (dimensionless) is the order of deactivation and *m* (dimensionless) measure the concentration dependency of the deactivation rate.

$$\begin{cases} r_{CO_2} = -k' \cdot C_{CO_2}^n \cdot a \\ \dfrac{da}{dt} = -k_d \cdot C_{CO_2}^m \cdot a^d \end{cases} \text{where } n = 1, m = 0 \text{ and } d = 1 \tag{9}$$

By integrating the 2nd equation of the system of equations (9) from the initial time (*t* = 0 h) to a generic time *t* (h) of the time-on-stream, equation (10) could be obtained; where a_0 is the initial activity that was always assumed unitary.

$$a(t) = a_0 \cdot e^{-k_d \cdot t} \tag{10}$$

By considering the design of the reactor and the experimental conditions, the solid phase could be assumed stationary, while the fluid phase could be assumed as a plug flow with constant flow rate [42]. Therefore, the performance equation of the process could be expressed as reported in equation (11), where V_{cat} (m^3) is the volume of the catalytic bed in the reactor.

$$\frac{V_{cat}}{\dot{n}_{CO_2,in}} = \int_{t=0}^{t} \frac{d\zeta_{CO_2}}{-r_{CO_2}} \tag{11}$$

By substituting r_{CO_2} with the 1st equation of the system of equations (9) and substituting the activity with the equation (10), equation (11) could be integrated and rearranged to obtain a linearised expression as reported in equation (12) [42]; where τ' (h) is the average residence time of the gas. This latter equation could be used to estimate the deactivation constant rate of each catalyst during the time-on-stream.

$$\ln\left[\ln\left(\frac{1}{1-\zeta_{CO_2}}\right)\right] = \ln(k' \cdot \tau') - k_d \cdot t \tag{12}$$

Lastly, the initial CO_2 conversion ($\zeta_{CO_2,0}$) obtained from this model could be estimated with equation (13) by assuming *t* = 0 h.

$$\zeta_{CO_2,0} = 1 - e^{-k' \cdot \tau'} \tag{13}$$

2.5 Kinetic analysis

To rationalise the results of the catalytic activity tests, the apparent activation energies for the CO_2 hydrogenation reactions to CO and methanol could be obtained from the catalytic tests at different reaction temperatures (200 – 300 °C). According to the 1st expression of the system of equations (9) the kinetic factor could be expressed according to the Arrhenius' equation as reported in equation (14). In this equation, R_i ($mol_i \cdot kg_{cat}^{-1} \cdot h^{-1}$) is the reaction rate, ρ_{cat} ($kg_{cat} \cdot m^{-3}$) is the catalytic bed density, $k'_{\infty,i}$ ($(mol_i \cdot m^{-3})^{1-n} \cdot h^{-1}$) is the pre-exponential factor, $E_{A,i}$ ($kJ \cdot mol^{-1}$) is the apparent activation energy, C_i ($mol_i \cdot m^{-3}$) is the concentration of the i-th compound, *n* (dimensionless) is the order of reaction with respect to the i-th species and $k^*_{\infty,i}$ ($mol_i \cdot kg_{cat}^{-1} \cdot h^{-1}$) represents the apparent pre-exponential factor.

$$R_i = r_i \cdot \rho_{cat}^{-1} = k'_{\infty,i} \cdot \exp\left(-\frac{E_{A,i}}{R \cdot T}\right) \cdot C_i^n \cdot \rho_{cat}^{-1} = k^*_{\infty,i} \cdot \exp\left(-\frac{E_{A,i}}{R \cdot T}\right) \tag{14}$$

The equation (14) could be linearised to obtain equation (15). Thus, the apparent pre-exponential factors and the apparent activation energies for each catalyst could be estimated by fitting the overall experimental reaction rates of CO_2, CO and methanol on the Arrhenius' plot.

$$\ln(R_i) = \ln\left(k^*_{\infty,i}\right) - \frac{E_{A,i}}{R} \cdot \frac{1}{T} \tag{15}$$

It is well known that the pre-exponential factor and the apparent activation energy are strongly correlated parameters. Hence, if the reaction mechanism on the different catalysts does not change significantly, a unique value of the apparent activation energy for all the catalysts can be determined for each reaction to decouple the two parameters. The objective function of this latter optimization is presented in equation (16), where $E_{A,i}$ ($kJ \cdot mol^{-1}$) is the apparent activation anergy of the i-th reaction (for the sake of clarity, *i* could be CO_2, CO or CH_3OH), $k^*_{\infty,i,j}$ ($mol_i \cdot kg_{cat}^{-1} \cdot h^{-1}$) is the apparent pre-exponential factor of the i-th reaction for the j-th catalyst, $T_{j,l}$ (K) is the l-th reaction temperature for the j-th catalyst and $R_{i,j,l,sp}$ ($mol_i \cdot kg_{cat}^{-1} \cdot h^{-1}$) is the experimental reaction rate of the i-th species for the j-th catalyst at the l-th reaction temperature.

$$f\left(E_{A,i}, k^*_{\infty,i,1}, \dots, k^*_{\infty,i,M}\right) = min \sum_{j=1}^{M} \sum_{l=1}^{L} \left\{\ln\left(R_{i,j,l,sp}\right) - \left[\ln\left(k^*_{\infty,i,j}\right) - \frac{E_{A,i}}{R} \cdot \frac{1}{T_{j,l}}\right]\right\}^2 \tag{16}$$

3 Results and Discussion

3.1 Physico-chemical characterization of the catalysts

All the catalysts were analysed with several characterization techniques to measure and evaluate different physico-chemical aspects that have been correlated to the synthesis technique and to the catalytic activity and stability. First of all, the elemental composition of the calcined samples was measured with ICP-MS, since the degree of hydration of two precursors was unknown, as reported previously in the methodology; for the sake of clarity, those nitrates were assumed trihydrate. The results in terms of the elemental composition of the calcined catalysts are detailed in Table S1, while Table 1 summarises the indium atomic content in the binary oxide samples. It is worth noting that the actual elemental composition of the In_xCe_{100-x} samples is close to the nominal one, while the elemental composition of the In_xZr_{100-x} samples differs uniformly from the nominal values. Hence, the hydration degree of the zirconyl nitrate was probably greater than the assumed value.

Table 1. Indium atomic content in the binary oxide calcined samples determined by means of ICP-MS measurements.

In/(In+M[a]) atomic ratio	Binary oxide catalysts					
	$In_{40}Ce_{60}$	$In_{60}Ce_{40}$	$In_{80}Ce_{20}$	$In_{40}Zr_{60}$	$In_{60}Zr_{40}$	$In_{80}Zr_{20}$
Nominal	0.40	0.60	0.80	0.40	0.60	0.80
Actual	0.39 ± 0.02	0.60 ± 0.02	0.85 ± 0.01	0.49 ± 0.01	0.71 ± 0.01	0.87 ± 0.01

[a] M represents respectively Ce or Zr in the In_xCe_{100-x} or In_xZr_{100-x} mixed catalysts.

The textural properties of both calcined and spent samples were evaluated by means of N_2 physisorption measurements; the results are summarised in Table 2. As far as the In_xCe_{100-x} catalysts are concerned, the specific surface area (S_{BET}, $m^2 \cdot g_{cat}^{-1}$) and the average pore size (d_p, nm) of the calcined samples did not show a clear trend, while the total pore volume (V_{BJH}, $cm^3 \cdot g_{cat}^{-1}$) slightly increases as the indium content rises. After the catalytic tests, the specific surface area of those samples approximately halved, while the mean pore size approximately doubled. On the contrary, both calcined and spent In_xZr_{100-x} samples exhibited a high specific surface area, showing a greater stability under reaction condition by increasing the zirconium content. It was also observed that the average pore size of those catalysts did not change significantly, while the total pore volume increased slightly during the catalytic tests. Overall, these results indicate that zirconium reduces sintering phenomena and stabilises the structure of the binary oxides better than cerium both during the preparation of the samples and during the catalytic tests. The latter is an important feature to keep high catalytic performances under reaction conditions.

Table 2. Textural properties of calcined and spent catalysts estimated by means of N_2 physisorption.

Catalyst	Calcined samples			Spent samples		
	S_{BET} ($m^2 \cdot g_{cat}^{-1}$)	V_{BJH} ($cm^3 \cdot g_{cat}^{-1}$)	d_p (nm)	S_{BET} ($m^2 \cdot g_{cat}^{-1}$)	V_{BJH} ($cm^3 \cdot g_{cat}^{-1}$)	d_p (nm)
Ce_{100}	59.6 ± 0.4	0.121	4.6	-	-	-
$In_{40}Ce_{60}$	41.3 ± 0.3	0.132	10.1	19.1 ± 0.2	0.122	21.8
$In_{60}Ce_{40}$	61.3 ± 0.3	0.159	8.2	26.7 ± 0.2	0.132	15.4
$In_{80}Ce_{20}$	55.6 ± 0.3	0.167	9.8	21.5 ± 0.2	0.132	20.3
In_{100}	35.6 ± 0.3	0.135	12.7	18.3 ± 0.1	0.137	29.4
$In_{80}Zr_{20}$	68.8 ± 0.2	0.160	7.2	51.1 ± 0.3	0.165	10.3
$In_{60}Zr_{40}$	63.8 ± 0.3	0.122	6.0	59.9 ± 0.4	0.124	6.2
$In_{40}Zr_{60}$	78.4 ± 0.2	0.129	5.2	68.8 ± 0.2	0.132	6.0
Zr_{100}	80.7 ± 0.3	0.091	3.4	-	-	-

The structural properties of the catalysts were investigated by using XRD. The X-ray diffractograms of the calcined and spent samples are shown in Figure S1 and in Figure 1, respectively. Concerning In_xCe_{100-x} samples, the diffraction peaks of the cubic structure of CeO_2 (PFD 01-081-0792) are clearly observable at 28.542°, 33.075°, 47.475° and 56.332°. Besides, the diffraction peaks of the cubic structure of In_2O_3 (PFD 03-065 -3170) are located at 21.448°, 30.515°, 35.380°, 50.901° and 60.517°. On the contrary, ZrO_2 is present as amorphous and non-crystalline form in the In_xZr_{100-x} samples: in fact, they exhibited two large halos located approximately between 25° and 35° and between 45° and 60°.

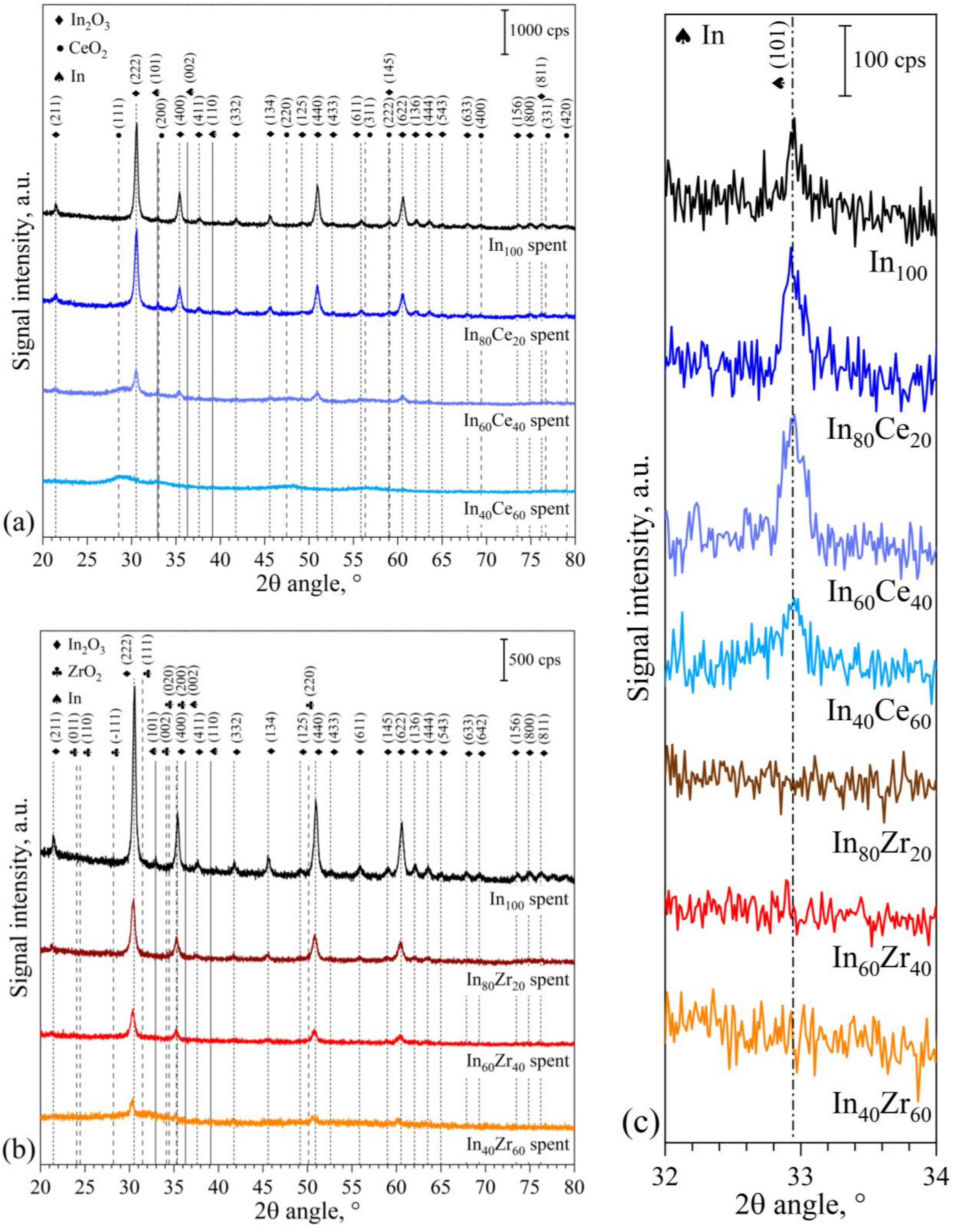

Figure 1. X-ray diffractograms of the spent (a) In$_x$Ce$_{100-x}$ and (b) In$_x$Zr$_{100-x}$ catalysts and (c) magnification of the XRD patterns of the spent samples between 32° and 34° of the 2θ angle.

The complete disappearance of the In_2O_3 peaks in the diffractogram of the $In_{40}Zr_{60}$ catalyst suggests that indium may be incorporated in the amorphous structure of zirconia, forming a solid solution of In_2O_3-ZrO_2 (see Figure S1). Metallic indium, Ce_2O_3 or sub-stoichiometric forms of ZrO_x were not detected by means of XRD in the calcined samples. A closer inspection of the diffractograms of the spent catalysts reported in Figure 1 reveals that the peaks of In_2O_3 and CeO_2 are more intense and narrower than the corresponding peaks in the calcined samples, suggesting that sintering phenomena occurred under catalytic tests. On the other hand, ZrO_2 remained amorphous without exhibiting clear detectable diffraction peaks. It is worth mentioning that the diffraction peaks of the tetragonal structure of the metallic indium (PFD 03-065-9682), located at 32.930°, 36.301° and 39.131°, were observed in the XRD patterns of the spent In_xCe_{100-x} samples (see Figure 1a), while they were not detected in the diffractograms of the spent In_xZr_{100-x} samples (see Figure 1b). In more detail, Figure 1c displays a magnification of the XRD patterns of the aged samples between 32° and 34°, showing the peak attributed to the Miller's indexes (101) of the metallic indium. This is a remarkable outcome that is related to the activity and stability of the binary oxides as described in more detail in the following paragraphs and in section 3.2.

As far as the crystalline structure is concerned, Table S2 summarises the average crystallite size, the lattice strain and the shift of the most intense peak of diffraction of each oxide phase. More specifically, what is interesting in this table is the growth of the crystallite size of In_2O_3 from ~3 nm to ~23 nm as the indium content in the calcined samples increases. Moreover, the average crystallite size of In_2O_3 rose by approximately 30% during the catalytic tests. Similarly, the average crystallite size of metallic indium in the spent In_xCe_{100-x} samples grew from 140 nm to 420 nm as the indium content increases. Regarding the size of the CeO_2 crystallites in the In_xCe_{100-x} samples, it remained steady at around 3 nm as the cerium content in the samples varied. Lastly, it is worth mentioning that the peaks of CeO_2, and in particular the more intense diffraction peak located at 28.542°, shift proportionally towards larger angles as the indium content in the sample rises. This positive shift has been ascribed to the formation of In-doped CeO_2 in which the indium atoms have an atomic radius smaller than the atomic radius of cerium [43]; indeed, the consequent shrinkage of ceria fluorite structure is responsible for the shift of XRD peaks [37]. On the contrary, Ce-doped In_2O_3 does not appear to be formed as the diffraction peaks of In_2O_3 do not shift.

The XRD outcomes were confirmed by Raman spectroscopy. In the Raman spectra of the mixed oxides (see Figure 2), the intense F_{2g} feature of CeO_2, associated with Ce-O symmetric stretching, is always present, while the typical vibrational modes of In_2O_3 were detected only in the samples presenting a high indium content [44]. The remarkable broadening of CeO_2 F_{2g} peak and its shift from 464 cm^{-1} to 454 cm^{-1} in the spectra of the In_xCe_{100-x} mixed oxides are likely due to the incorporation of indium ions into ceria lattice, confirming the formation of an In-doped CeO_2 phase. Consistently, a significant increase of CeO_2 defect band was observed in the presence of In, as also proved by the increase of the D/F_{2g} area ratio. This parameter, calculated as the ratio between the area of the broad defect-induced band around 600 cm^{-1} and the area of the main F_{2g} peak, is widely employed to estimate defect abundance in ceria-based samples. An attempt was also made to semi-quantitatively evaluate the defect abundance in the In_2O_3 structure [29]. Since Gan et al. [45] correlated the intensity of the Raman feature at 367 cm^{-1} to the presence of oxygen vacancies in indium oxide, we calculated the ratio between the areas of this component and the one of the main In_2O_3 peak at 308 cm^{-1}; due to the too low intensity of these peaks in the Ce-rich materials, this calculation was only possible for the In_{100} and $In_{80}Ce_{20}$ samples. The area ratio increases upon Ce addition and after the catalytic tests, suggesting that more oxygen defects form in the In_2O_3 structure.

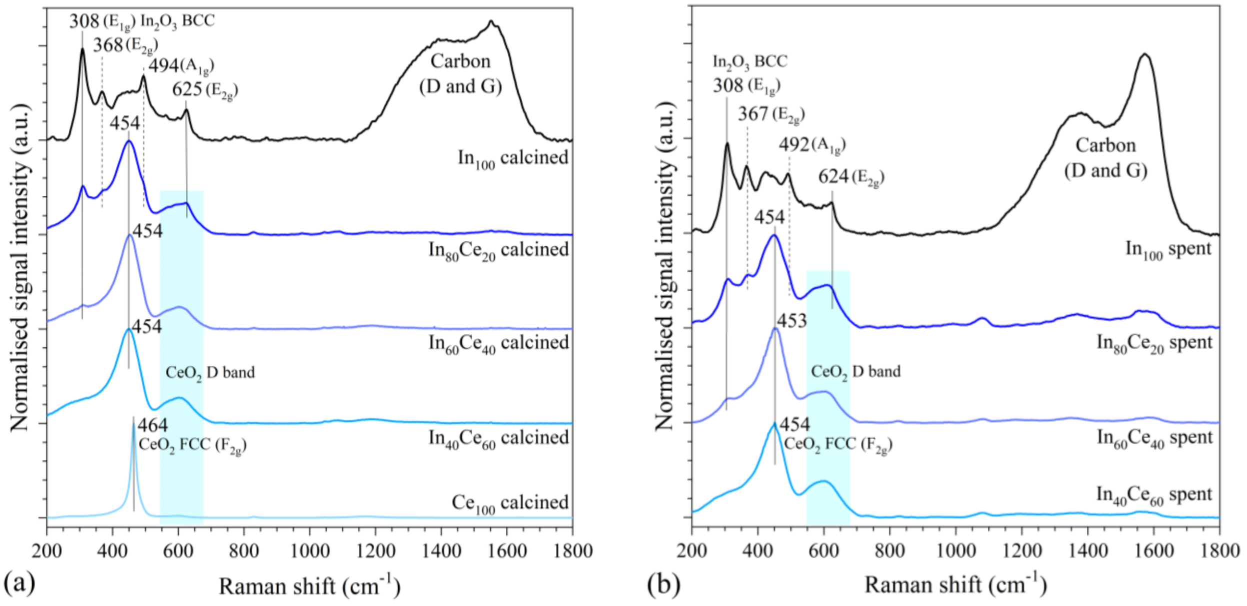

Figure 2. Raman spectra of (a) calcined and (b) spent In_xCe_{100-x} samples. For the sake of clarity, the signals were normalised with respect to the F_{2g} peak, except for the In_{100}, where the E_{1g} peak was used [44].

As aforementioned, metallic indium was detected only in the spent In_xCe_{100-x} samples by means of XRD measurements, as can be clearly seen in Figure 1c. Moreover, what stands out in Figure 3 is that the H_2-TPR measurements confirmed the increased reducibility of those catalysts in a range of temperature that is consistent with the reaction conditions. More specifically, the total H_2 consumption for the In_xCe_{100-x} samples rises linearly from 1.06 $mmol_{H2}\cdot g_{cat}^{-1}$ to 11.1 $mmol_{H2}\cdot g_{cat}^{-1}$ as the indium content grows from 0 at.% to 100 at.%. In Figure 3b, the low-temperature peaks at 268 °C, 292 °C and 344 °C correspond respectively to the 1.7%, 6.8% and 15.1% of the total H_2 consumption of each sample. This means that the amount of reduced In_2O_3 at low temperature increases by reducing its content in the catalysts, causing a loss of active phase under reaction conditions as discussed in the next section. Concerning the In_xZr_{100-x} binary oxides, their total H_2 consumption (i.e., 9.3 $mmol_{H2}\cdot g_{cat}^{-1}$ for $In_{40}Zr_{60}$, 15.2 $mmol_{H2}\cdot g_{cat}^{-1}$ for $In_{60}Zr_{40}$ and 17.3 $mmol_{H2}\cdot g_{cat}^{-1}$ for $In_{80}Zr_{20}$) is greater than the one of the In_xCe_{100-x} binary oxides, suggesting that the addition of zirconium also increases the reducibility of In_2O_3; however, it seems to stabilise the structure because the reduction of In_2O_3 occurs at temperatures higher than the reaction temperature of the catalytic tests. Accordingly, as presented in Figure 1c, no metallic indium was detected in the spent In_xZr_{100-x} samples. This is an important aspect because the formation of metallic indium in the In_xCe_{100-x} binary oxides could be directly related to the progressive deactivation of the samples as described more specifically in section 3.2.

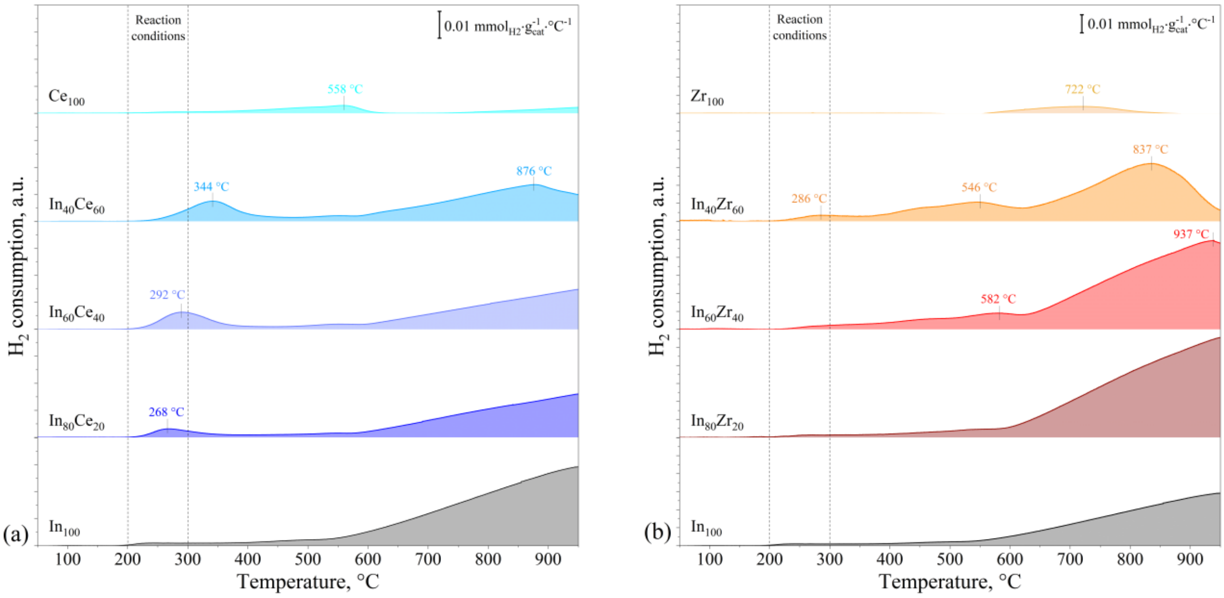

Figure 3. H_2-TPR of the calcined samples: (b) In$_x$Ce$_{100-x}$ and (c) In$_x$Zr$_{100-x}$.

Moving on now to consider the results of the CO_2-TPD, Figure 4 displays the CO_2-TPD profiles of the spent samples. It is apparent from these profiles that the strength of the basic sites on the surface of the catalytic material changes completely in the In$_x$Zr$_{100-x}$ samples. The amount of CO_2 desorbed at high temperature (T > 700 °C) increases from 0.29 mmol$_{CO2}$/g$_{cat}$ to 2.55 mmol$_{CO2}$/g$_{cat}$ by growing the ZrO_2 content in the catalysts; however, at these high temperatures the signal may be disturbed by the release of oxygen from the surface, that was not observed in the other samples. On the other hand, the addition of CeO_2 in the samples slightly reduces the strength of the CO_2 bonds with the superficial sites. The different desorption temperature could be related to the different chemisorbed species such as bicarbonate, bidentate- or tridentate-like carbonate species [46]. For the sake of completeness, Figure S2 shows the CO_2-TPD measurements of the calcined samples. It is worth noting that all the samples desorbed CO_2 at low temperature, but this feature changes in the spent catalysts probably due to the prolonged exposition to reaction conditions. Both calcined and spent samples desorbed the main amount of CO_2 between 400 °C and 600 °C.

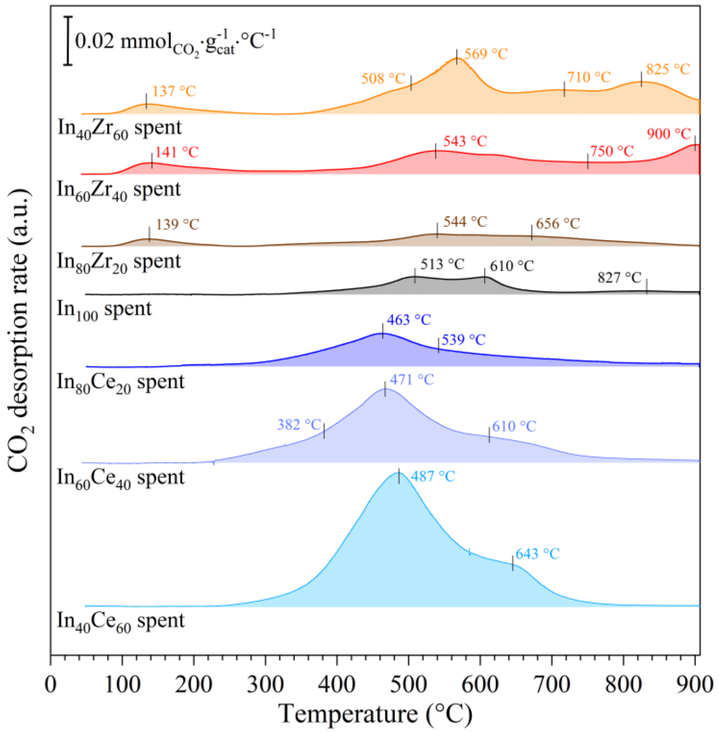

Figure 4. CO_2-TPD of the spent In_xCe_{100-x} and In_xZr_{100-x} catalysts.

Furthermore, as shown in Figure 5a, the desorbed amount of CO_2 increases proportionally as the indium content diminishes for both the binary oxides groups. In support of this result, XPS measurements were performed on the spent samples (see Figure S3, Figure S4, Figure S5 and Figure S6). As shown in Figure S3 and Figure S4, the XPS HR spectra for the O1s and the C1s signals exhibited respectively a peak located at ~531.7 eV and a peak located at ~289 eV that grew by reducing the indium content in the samples. These signals have been ascribed to the presence of carbonates and to the organic C=O bond [47]. In fact, as shown in Figure 5b, the amount of CO_2 desorbed seems to be related to the fraction of the deconvoluted peak of the O1s signal located at ~531.7 eV. Moreover, as reported in the literature, a peak of the O1s signal located at ~532.5 eV could be related to the presence of hydroxyl species [46,48]; whereas a peak located at ~530.5 eV was attributed to O defects [26,46,48]. The presence of both hydroxyl groups and carbonates was confirmed by means of FT-IR measurements on the In_xZr_{100-x} samples as illustrated in Figure S7 and Figure S8. A closer inspection of the spectra revealed that the wide band between 3700 cm^{-1} and 2900 cm^{-1} is commonly attributed to the stretching vibrations of the hydroxyl groups of adsorbed water molecules [49]. Besides, the peaks located at ~1545 cm^{-1} and ~1370 cm^{-1} have been ascribed to the presence of carbonates on the surface [50,51]. Lastly, the narrow peak located at 2337 cm^{-1} may be assigned to gaseous CO_2 trapped in closed channels [51] of the samples or to stretching vibrations of the Zr-OH bonds [52,53].

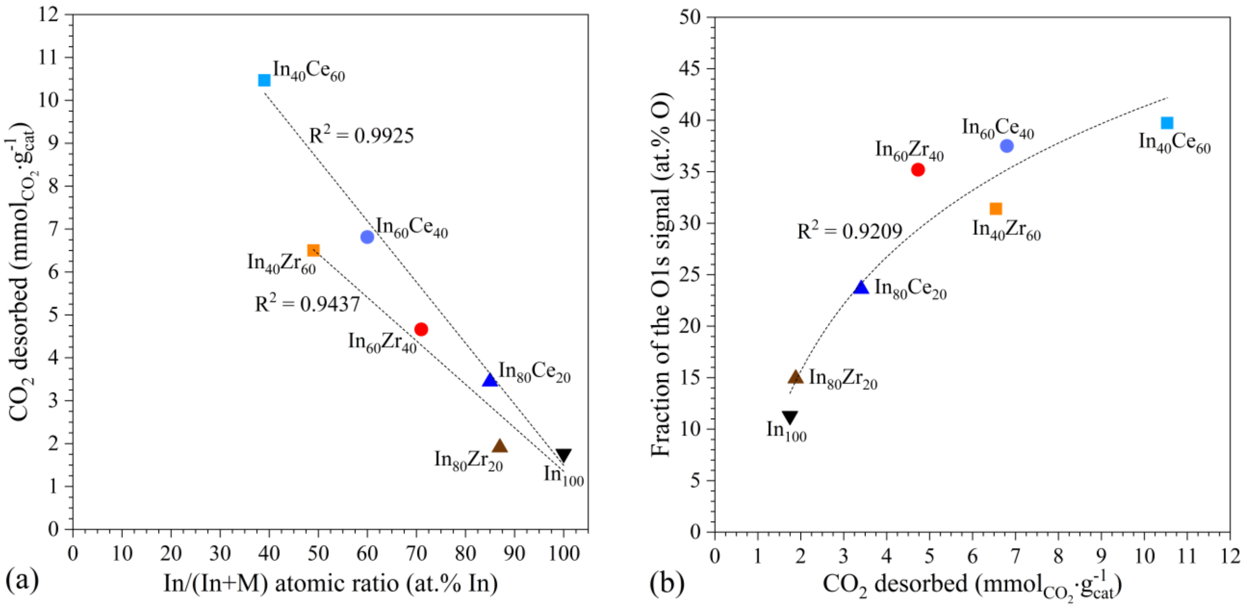

Figure 5. (a) Relationship between the indium content estimated by using ICP-MS (M represents Ce or Zr, see Table 1) and the CO_2 desorbed during the CO_2-TPD of the spent catalysts. (b) Relationship between the desorbed amount of CO_2 during the CO_2-TPD and the fraction of the O1s signal located at ~531.7 eV obtained from the deconvolution of the XPS HR spectra (see Figure S3).

Further XPS HR spectra were collected for the In3d, Ce3d and Zr3d peaks of the spent catalysts and the results are shown in Figure S5, Figure S6a and Figure S6b, respectively. Concerning the In3d signals of the In_xCe_{100-x} samples, it is evident that there are no differences at the variation of the indium content. On the other hand, a small shift from 444 eV to 444.6 eV of the $In3d_{5/2}$ of the In_xZr_{100-x} samples binding energy occurred by reducing the indium content; according to the literature, it may be related to the formation of chemisorbed species that participate into the overall CO_2 hydrogenation reaction pathway. Loh and Kerani (2019) have suggested that a possible reaction pathway on the surface of $In_2O_{3-x}OH_y$ may involve the filling of an oxygen vacancy to form a bidentate-like carbonate with a C-O bond that may be activated by a neighbouring hydride species to form a formate group [46]. Moreover, the formation of In-C bonds in the spent In_xZr_{100-x} samples was detected by means of XPS, suggesting that the formation of oxygen defects (or vacancies) could be filled by CO_2 forming a bidentate-like carbonate [26,46]. Lastly, the XPS HR spectra for the Ce3d and the Zr3d peaks of the spent binary oxides were deconvoluted to estimate the average oxidation state and the results will be further discussed in section 3.3.

Before proceeding to examine the catalytic performances of the binary oxide catalysts, another significant aspect is the morphology of the samples. The different morphological nature of the two groups of catalysts is clearly exemplified in Figure 6. The spent In_{100} catalyst is made up of agglomerates of particles and it is evident that the structure of the material is not completely different from the calcined In_{100} sample (see Figure S9a). The size of the particles of the spent In_{100} sample ranges from ~15 nm to ~40 nm, which is consistent with the average crystallite size estimated by means of XRD measurements (see Table S2). As far as the In_xCe_{100-x} samples are concerned, they showed a mesoporous sponge-like structure, that thickens by increasing the Ce content. The very small round-shaped particles have been assigned to CeO_2, while the more regular and larger crystals have been attributed to the cubic structure of In_2O_3. On the other hand, In_xZr_{100-x} samples have a completely different structure. Concerning the calcined samples, $In_{80}Zr_{20}$ and $In_{60}Zr_{40}$ showed a lamellar-like structure, while $In_{40}Zr_{60}$ is characterised by intertwined fibres on which aggregates of small particles are dispersed, as illustrated in Figure S9. The spent catalysts are made of a fibrous structure decorated with In_2O_3 crystals (see Figure 6e-g). The morphology of those samples changes completely under reaction conditions.

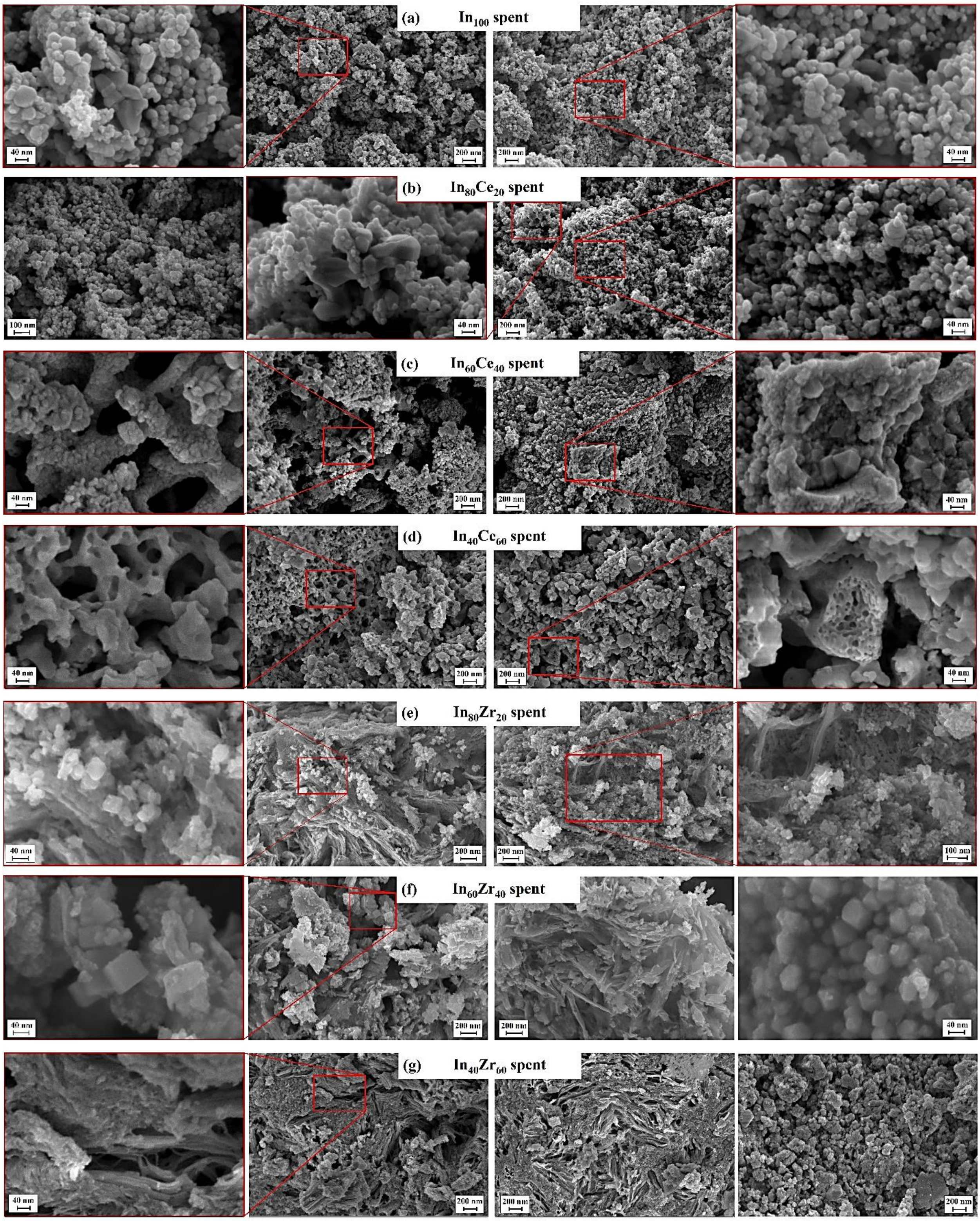

Figure 6. FE-SEM images of the spent catalysts: (a) In_{100}, (b) $In_{80}Ce_{20}$, (c) $In_{60}Ce_{40}$, (d) $In_{40}Ce_{60}$, (e) $In_{80}Zr_{20}$, (f) $In_{60}Zr_{40}$ and (g) $In_{40}Zr_{60}$.

3.2 *Catalytic stability*

So far, this paper has focused on the results of the characterisation techniques. The following section will present the results of the stability tests performed on the binary oxide catalysts, attempting to provide an explanation to the behaviour of the catalytic performances. Before proceeding to examine the stability tests, it is important to restate that, prior to the tests, each catalyst was pre-treated in pure nitrogen at 300 °C for 1 h, then it was subjected to the 20-h stability test at 275 °C, 2.5 MPa, and 20 $NL \cdot g_{cat}^{-1} \cdot h^{-1}$ (inlet gas composition: 60 vol.% H_2, 20 vol.% CO_2 and 20 vol.% N_2). The experimental results are shown in Figure 7. The In_xZr_{100-x} catalysts exhibited a CO_2 conversion rate higher than pure In_2O_3, showing that the addition of zirconium promotes the CO_2 hydrogenation reactions. On the contrary, In_xCe_{100-x} binary oxides exhibited a fall of the CO_2 conversion rate caused by the addition of cerium in the samples. As shown in Figure 7b, the In_xCe_{100-x} catalysts exhibited a methanol selectivity greater than the In_xZr_{100-x} catalysts, but the methanol yield of the In_xZr_{100-x} catalysts remained superior. Overall, the activity of the samples will be discussed in more detail in the next section; so, focusing now on the stability of the samples, Figure 7a reveals a progressive loss of activity under reaction conditions. The deactivation is caused by several phenomena, more precisely, it may be ascribed to those listed below:

- a loss of the active surface area due to the shrinkage and the rearrangement of the structure,
- sintering of the particles that leads to a reduction of the dispersion of the active phase,
- the formation of metallic indium that results in a gradual decline of the active surface area,
- coking of the active surface area caused by the deposition of carbon species.

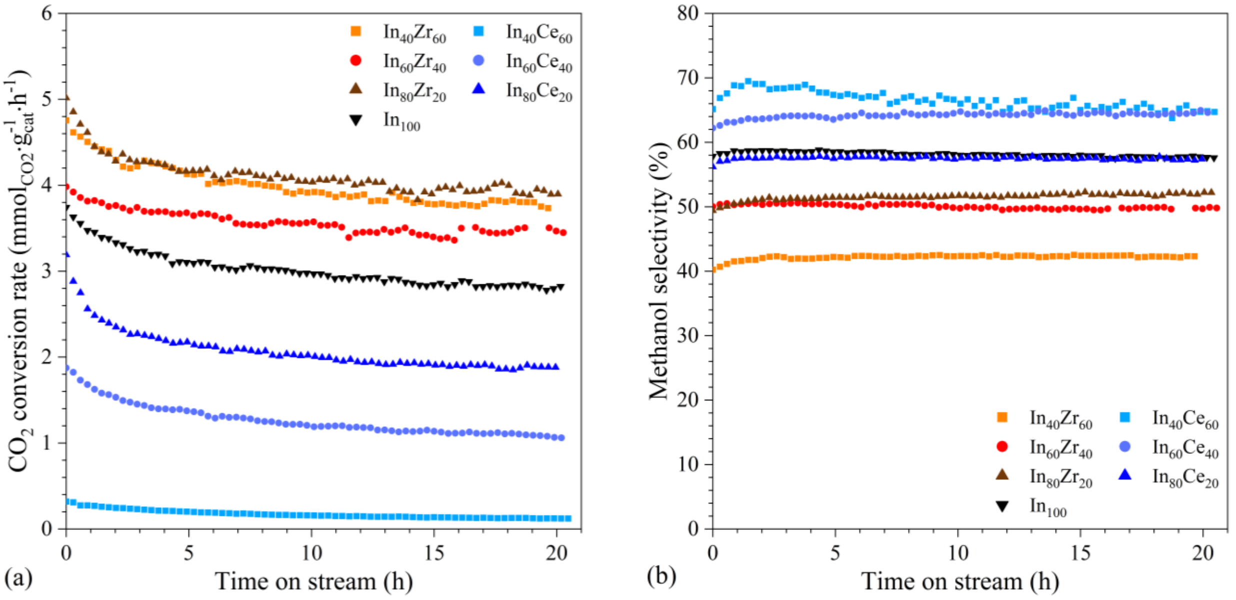

Figure 7. (a) CO_2 conversion rate and (b) methanol selectivity of the In_xCe_{100-x} and In_xZr_{100-x} catalysts during the 20-h stability test. Reaction conditions are 275 °C, 2.5 MPa and 20 $NL\cdot g_{cat}^{-1}\cdot h^{-1}$ (inlet gas composition: 60 vol.% H_2, 20 vol.% CO_2 and 20 vol.% N_2).

For the purpose of rationalising the causes of the deactivation, the CO_2 conversion profiles were fitted by using the equation (11) and the deactivation parameters are summarised in Table 3. What stands out from the table is the growth of the deactivation constant by increasing the cerium content in the samples. These results further support the idea that the addition of CeO_2 reduces the stability of the samples, while ZrO_2 stabilises the binary oxide structure and increases the overall activity in CO_2 hydrogenation.

Table 3. Deactivation parameters of the 1st order deactivation rate at 275 °C.

Catalyst	Deactivation constant (k_d), h^{-1}	$\ln(k'\cdot\tau')$, dimensionless	Correlation coefficient (R^2)
$In_{40}Ce_{60}$	$(4.13 \pm 0.13) \cdot 10^{-2}$	-6.553 ± 0.016	0.9308
$In_{60}Ce_{40}$	$(2.14 \pm 0.10) \cdot 10^{-2}$	-4.736 ± 0.012	0.8713
$In_{80}Ce_{20}$	$(1.60 \pm 0.11) \cdot 10^{-2}$	-4.293 ± 0.013	0.7476
In_{100}	$(1.04 \pm 0.06) \cdot 10^{-2}$	-3.963 ± 0.007	0.8361
$In_{80}Zr_{20}$	$(7.41 \pm 0.56) \cdot 10^{-3}$	-3.684 ± 0.007	0.7168
$In_{60}Zr_{40}$	$(5.48 \pm 0.36) \cdot 10^{-3}$	-3.846 ± 0.004	0.7657
$In_{40}Zr_{60}$	$(9.28 \pm 0.48) \cdot 10^{-3}$	-3.694 ± 0.006	0.8474

Moreover, the CO_2 conversion profiles showed a steep drop during the initial part of the tests, that might be caused by the reduction of the specific surface area and by the sintering of the particles. Hence, a reasonable approach to tackle this issue could be to find a relationship between the drop of the activity during the initial part of the stability test and the reduction of specific surface area measured by using N_2 physisorption. More precisely, as illustrated in Figure 8, the reduction of the specific surface area of all the samples (see Table 2) seems to be correlated to the sharp fall of CO_2 conversion during the stability tests. This finding could provide an explanation to the behaviour of the catalysts during the initial part of the stability test; however, they reveal that a progressive decline of the CO_2 conversion rate during the time on stream may be attributed to other causes.

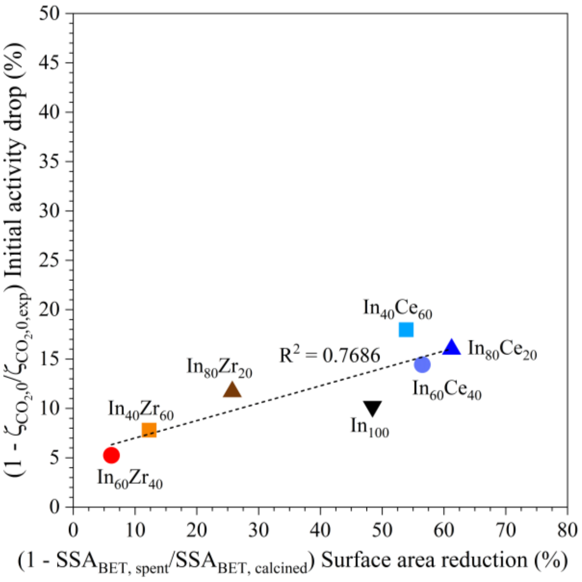

Figure 8. Relationship between the reduction of specific surface area during the catalytic tests under reaction conditions and the initial drop of activity during the stability test carried out at 275 °C. For the sake of clarity, $\zeta_{CO_2,0}$ was estimated by using equation (13); while $\zeta_{CO_2,0,exp}$ is the initial experimental CO_2 conversion.

As previously shown in Figure 3a, the spent In_xCe_{100-x} samples contain metallic indium. The semi-quantitative analysis of the X-ray diffractograms of the samples allowed to estimate the mass fraction of metallic indium compared to the total amount of indium and indium oxide in the samples. In more detail, the mass fraction of In_2O_3 reduced into metallic indium was 50%, 25%, 9% and 4% for the $In_{40}Ce_{60}$, $In_{60}Ce_{40}$, $In_{80}Ce_{20}$ and In_{100}

samples, respectively. Moreover, the H_2-TPR measurements revealed that the addition of CeO_2 increases the reducibility of the binary oxides at low temperatures (i.e., between 200 °C and 300 °C). Therefore, the relationship shown in Figure 9a demonstrates that the amount of metallic indium formed under reaction conditions depends directly on the reducibility at low temperature of the samples. This finding provides some tentative evidence that the reduction of In_2O_3 into metallic indium is a phenomenon slower than the loss of specific surface area and it is likely related to the gradual deactivation of the samples. Figure 9b displays indeed the relationship between the reducibility of the In_xCe_{100-x} samples and the deactivation constant at 275 °C. What is striking from those two correlations is that the reducibility at low temperature of the samples grows as the cerium content rises and promotes the formation of metallic indium on the surface of the samples, that leads to a continuous decreasing of the performances of the In_xCe_{100-x} catalysts. Concerning the In_xZr_{100-x} catalysts, the experimental evidence showed that ZrO_2 increases slightly the reducibility of the oxides at high temperatures, in fact, no metallic indium was detected in the spent catalysts. This result confirms that the deactivation of In_xZr_{100-x} samples is not linked to their reducibility.

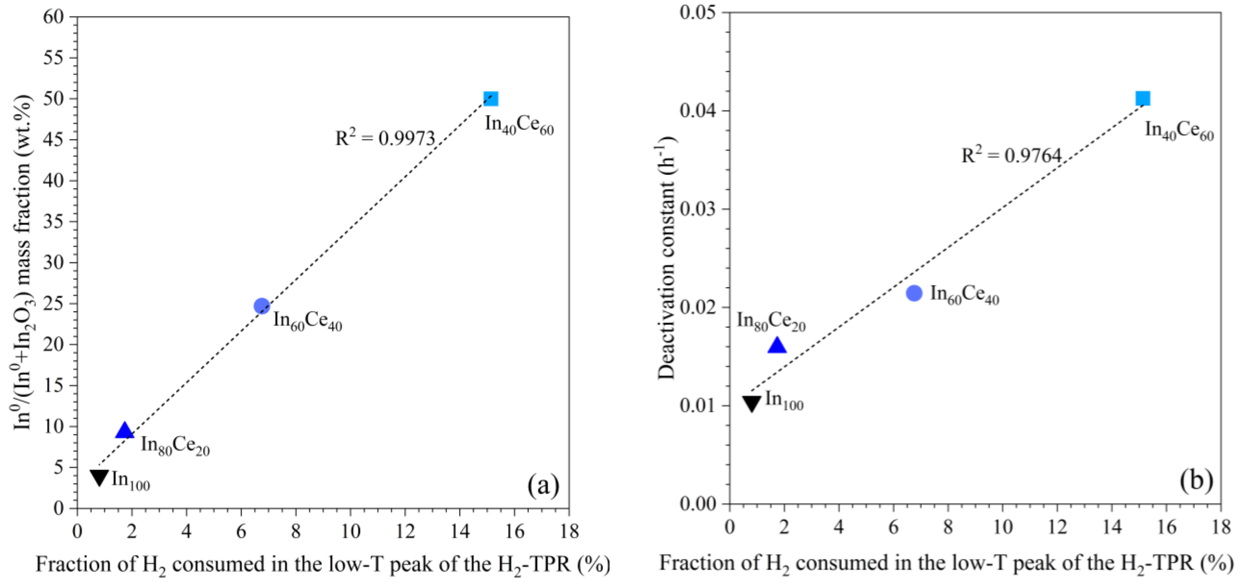

Figure 9. (a) Relationship between the fraction of H_2 consumed in the low-temperature peak of the H_2-TPR profiles and the mass fraction of metallic indium in the spent samples obtained by means of XRD. (b) Relationship between the fraction of H_2 consumed in the low-temperature peak of the H_2-TPR profiles and the deactivation constant at 275 °C for the In_xCe_{100-x} samples.

Another possible cause of deactivation could be coking. TPC is a suitable characterisation technique of the spent catalysts to quantify the amount of carbon deposited on the surface of the samples during the catalytic tests. Figure 10 illustrates the relationship between the amount of CO_x produced during the TPC and the deactivation constant at 275 °C of the samples. What is interesting about the data in this figure is that the two variables are clearly correlated to each other in the case of the In_xCe_{100-x} catalysts, whereas the deactivation constant of In_xZr_{100-x} catalysts seems to be independent on the carbon deposition. More specifically, the deactivation constant increases as the CeO_2 concentration in the sample grows.

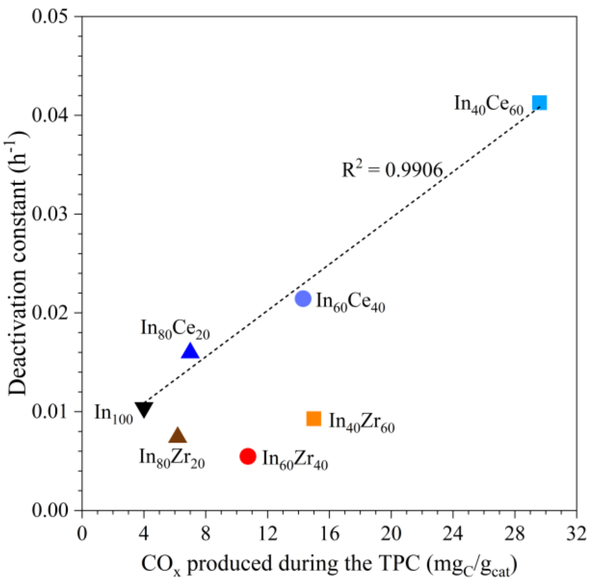

Figure 10. Relationship between the amount of CO and CO_2 produced during the TPC and the deactivation constant at 275 °C.

In summary, this section of the manuscript has attempted to provide an explanation to the deactivation phenomena that occur on those catalysts during the CO_2 hydrogenation to methanol. It is worth noting that all the samples seem to be severely affected by the reduction of the specific surface area during the initial part of the test. Subsequently, In_xZr_{100-x} binary oxide catalysts reach steady performances at 275 °C with a low deactivation constant and they did not seem to be affected by other deactivating phenomena. On the contrary, the continuous decrease of the performances of the In_xCe_{100-x} binary oxide catalysts suggested that deactivation phenomena slower than the structural shrinkage occurred. The reduction of In_2O_3 to metallic indium and the carbon deposition were indeed the phenomena that almost certainly deactivated the samples.

3.3 *Catalytic activity*

As far as the catalytic activity tests are concerned, they were carried out at 2.5 MPa, 20 $NL \cdot g_{cat}^{-1} \cdot h^{-1}$ (inlet composition: 60 vol.% H_2, 20 vol.% CO_2 and 20 vol.% N_2), varying the reaction temperature between 200 °C and 300 °C. Supplementary Figure S10 illustrates the catalytic performance with respect to the mass of catalyst in the catalytic bed. From these results it is evident that the CO_2 conversion increases as the temperature rises as a consequence of the increase of the reaction rate and it could be stated that the activity of the In_xCe_{100-x} samples decreases by reducing the indium content; whilst there is not a clear trend for the In_xZr_{100-x} samples. To understand the effects of the addition of ZrO_2 or CeO_2 to In_2O_3, Figure 11 displays the catalytic results with respect to the actual mass of In_2O_3 in each sample.

Concerning the In_xCe_{100-x} samples, the specific CO_2 conversion rate in Figure 11a decreases proportionally as the indium content diminishes, suggesting that the activity of In_2O_3 is worsened by the addition of CeO_2. On the contrary, In_xZr_{100-x} samples exhibited a specific CO_2 conversion rate greater than the one of the pure In_2O_3 sample. Moreover, the specific methanol productivity (see Figure 11b) is also enhanced by the addition of ZrO_2 in the catalysts. Those results are consistent with the findings of Martin *et al.* [26]. The CO_2 hydrogenation to methanol is indeed boosted by the formation of oxygen vacancies on the surface of In_2O_3, that is promoted by the presence of ZrO_2 [25,26]. The $In_{40}Zr_{60}$ catalyst reached a specific methanol productivity of 168 $mg_{CH3OH} \cdot g_{In2O3}^{-1} \cdot h^{-1}$ at 300 °C, while its methanol selectivity fell from 81.2 % at 200 °C to 28.3 % at 300 °C. However, as previously discussed, In_xCe_{100-x} samples were subjected to a significant reduction of the specific surface area, while In_xZr_{100-x} catalysts kept a high specific surface area under reaction condition. Thus, pure In_2O_3 showed the best specific methanol productivity per unit of surface area (i.e., 5.32 $g_{CH3OH} \cdot m_{cat}^{-2} \cdot h^{-1}$ at 300 °C) followed by the $In_{80}Ce_{20}$ sample (i.e., 3.27 $g_{CH3OH} \cdot m_{cat}^{-2} \cdot h^{-1}$ at 300 °C) and the $In_{80}Zr_{20}$ sample (i.e., 2.23 $g_{CH3OH} \cdot m_{cat}^{-2} \cdot h^{-1}$ at 300 °C). Finally, it is worth mentioning that In_xZr_{100-x} catalysts produced small amounts of dimethyl-ether as a by-product due to the surface acidity of ZrO_2, which promotes the dehydration of methanol to dimethyl-ether. The dimethyl-ether yield was 0.026%, 0.037% and 0.024% for the $In_{40}Zr_{60}$, $In_{60}Zr_{40}$ and $In_{80}Zr_{20}$ catalysts, respectively.

Besides temperature, pressure is the other significant parameter of the methanol synthesis process. The latter indeed occurs with a reduction of the number of moles as shown in equations (1) and (2), and according to the Le Châtelier-Braun principle, methanol is a thermodynamically favoured product by the increase of pressure. On the contrary, the RWGS reaction is not affected by the variation of the pressure. For these reasons, an increase of the partial pressure of the reactants has a beneficial effect on the methanol selectivity; in fact, Martin *et al.* [26] reported that the methanol selectivity approaches to 100% at 50 bar. Moreover, an increase of the pressure promotes the reaction rates and increase the overall CO_2 conversion.

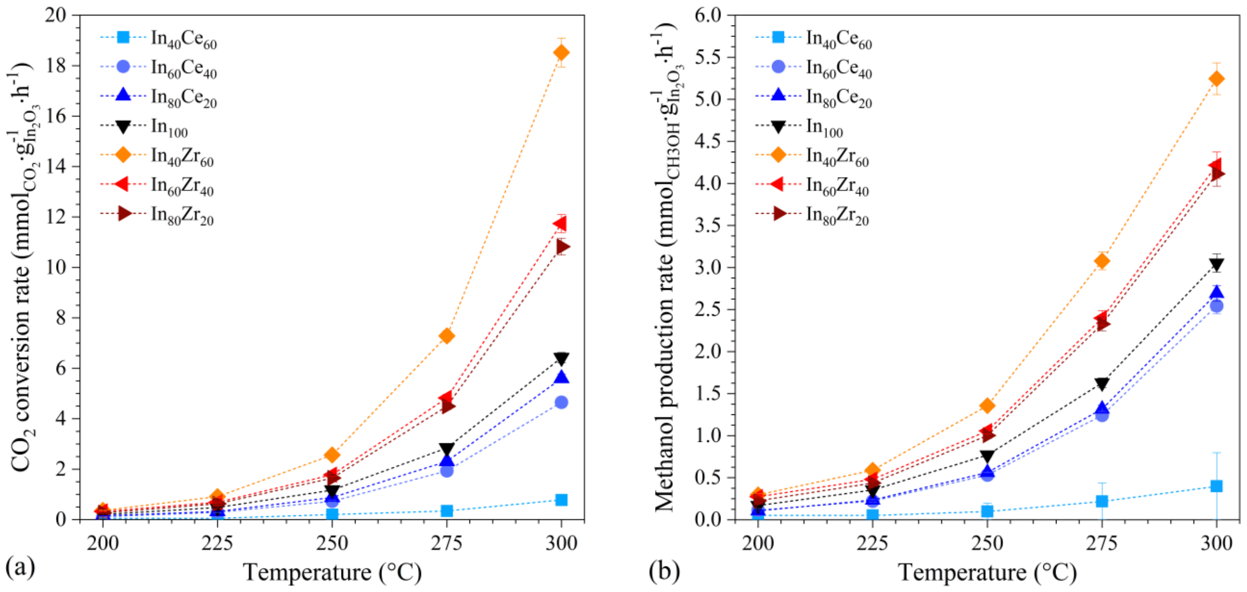

Figure 11. (a) Specific CO_2 conversion rate and (b) specific methanol production rate of the In_xCe_{100-x} and In_xZr_{100-x} binary oxide catalysts. Reaction conditions are 2.5 MPa and 20 $NL \cdot g_{cat}^{-1} \cdot h^{-1}$ (inlet composition: 60 vol.% H_2, 20 vol.% CO_2 and 20 vol.% N_2). For the sake of clarity, the actual mass fractions of In_2O_3 estimated by means of ICP-MS measurements were used in the calculation of the specific CO_2 conversion rate.

As aforementioned, the performances of indium-based catalysts strongly depend on the presence of oxygen vacancies; thus, to rationalise those intriguing findings related to the activity of the samples, we performed XPS and Raman spectroscopy. The most significant results of those measurements are presented in Table 4, while more detailed data are reported in Figure 2 and in the Supplementary Material (see Figure S5, Figure S6, Figure S7 and Figure S8). Firstly, the superficial indium atomic ratio was estimated by using XPS and it is worth noting that indium concentration on the surface of the In_xCe_{100-x} samples is higher than the one of the In_xZr_{100-x} catalysts. In addition, if it is compared with bulk values obtained by means of ICP-MS measurements (see Table 1), it is evident that the addition of CeO_2 increases the surface concentration of indium atoms. The average oxidation state of indium estimated by using the modified Auger parameter is +3 in all the spent samples. On the other hand, the average oxidation state of Ce estimated from the deconvolution of the Ce3d signals of the In_xCe_{100-x} samples (see Figure S6a) decreases by rising the cerium content in the sample demonstrating the increase in reducibility and the presence of Ce^{+3}. Whereas the average oxidation state of Zr estimated from the deconvolution of the Zr3d signals in the In_xZr_{100-x} samples (see Figure S6b) is low, suggesting the presence of Zr sub-oxides (ZrO_x with $x < 2$).

The concentration of oxygen defects was estimated from the deconvolution of the O1s signals of the XPS measurements and from Raman spectroscopy. Concerning In_xCe_{100-x} samples, the deconvolution of the O1s signal revealed that the concentration of oxygen defects increases from 14.0 at.% of the $In_{80}Ce_{20}$ to 21.6 at.% of the $In_{40}Ce_{60}$ and this result is consistent with the Raman measurements. In more detail, the D/F_{2g} ratio of the In_xCe_{100-x} samples is 0.03 for the calcined Ce_{100} powder, it is almost constant for the calcined binary oxides (0.32 – 0.33) and increases up to 0.53 – 0.56 for all the spent catalysts. These data appear to support the idea that oxygen defects are mainly linked to the cerium oxide rather than to the indium oxide. Therefore, the addition of Ce in the samples increased the concentration of O defects in the CeO_2 structure and the reducing atmosphere amplified the presence of O defects in the spent samples. Hence, the O defects in the In_xCe_{100-x} samples seems to be more correlated to the deactivation phenomena rather than the activity. In fact, if the concentration of O defects increased in the CeO_2 phase while the In_2O_3 phase was only marginally affected by this phenomenon, the activity in CO_2 hydrogenation would decrease as the indium content diminished.

On the other side, In_xZr_{100-x} samples appear to exhibit a different behaviour. Similar to the In_xCe_{100-x} samples, the concentration of O defects in the spent In_xZr_{100-x} samples increases from 12.6 % for $In_{80}Zr_{20}$ to 21.1 % for $In_{40}Zr_{60}$. However, the average oxidation state of Zr is significantly lower than the average oxidation state of Ce. Hence, the O defects may also affect the In_2O_3 and not only the zirconium oxide. In support of this interpretation, Martin *et al.* [26] have attributed the formation of O defects (and/or O vacancies) to the electronic promotion of Zr cations that change their oxidation state from +4 to +3, favouring the formation of other O defects in the In_2O_3 structure. Consequently, the increase of O defects in the indium oxide led to an increase of the catalytic activity in CO_2 hydrogenation.

Table 4. Results of XPS and Raman measurements on the spent samples.

Sample	In/(In+M)[a]	In Auger parameter[b]	M^{4+}/M[c]	O_{defect}/O[d]	D/F_{2g} area ratio[e]
	at. %	eV	at. %	at. %	-
$In_{40}Ce_{60}$	47.4	850.9	56.7	21.6	0.56
$In_{60}Ce_{40}$	75.2	851.0	64.3	14.9	0.53
$In_{80}Ce_{20}$	93.5	850.7	67.3	14.0	0.54
In_{100}	100	850.7	-	17.1	-
$In_{80}Zr_{20}$	80.0	851.2	15.2	12.6	-
$In_{60}Zr_{40}$	70.2	850.4	30.4	17.5	-
$In_{40}Zr_{60}$	44.0	850.7	21.6	21.1	-

[a] Elemental atomic ratio on the surface of the samples estimated by means of XPS measurements. For the sake of clarity, M represents respectively Ce or Zr in the samples.

[b] Modified Auger parameter of indium estimated by using the In MNN signals of the XPS measurements.

[c] Fraction of Ce^{4+} or Zr^{4+} species with respect to Ce or Zr species estimated by means of the deconvolution of the Ce3d or Zr3d signals of the XPS measurements (see Figure S6).

[d] Fraction of O_{defect} species with respect to O species estimated by means of the deconvolution of the O1s signal of the XPS measurements (see Figure S3).

[e] Defects in the CeO_2 structure estimated by means of Raman spectroscopy (see Figure 2b).

To investigate if the reaction mechanism changes on the surface of the two catalytic groups, the experimental reaction rates were fitted on the Arrhenius' plot (see Figure S11, Figure S12 and Figure S13) and the results are reported in Table S3. What stands out from the table is that the apparent activation energies for the CO_2 hydrogenation ranges between 66 $kJ \cdot mol^{-1}$ and 89.9 $kJ \cdot mol^{-1}$ with a relative uncertainty that achieves 15.2 % in the worst case (i.e., $In_{40}Ce_{60}$). Moreover, according to the literature [54], the apparent activation energy for CO synthesis is greater than the one for the methanol synthesis. In addition, it is worth noting that the pre-exponential factors and the activation energies are strongly dependent on each other; however, for each reaction the apparent activation energy does not seem to change significantly. For these reasons, the pre-exponential factors and the apparent activation energies were determined by assuming that the apparent activation energy of each reaction is the same for all the samples and the results are summarised in Table 5. What stands out from the table is that the apparent activation energy of the methanol synthesis (65.5 kJ·mol^{-1}) is lower than the one of the RWGS reaction (107.5 kJ·mol^{-1}), while the apparent activation energy for the CO_2 hydrogenation is about 81.0 kJ·mol^{-1}. A closer inspection of the pre-exponential factors revealed that the addition of CeO_2 progressively reduces the number of active sites and consequently the performance of the In_xCe_{100-x} samples. On the other hand, the pre-exponential factors of the In_xZr_{100-x} samples do not seem to change at the variation of the ZrO_2 content; therefore, this feature resulted in a higher specific activity (i.e., number of active sites) of this group of catalysts. In conclusion, these findings are consistent with the previous results of the characterisations and the higher performances of the In_xZr_{100-x} samples could be almost certainly ascribed to the electronic promotion of Zr.

Table 5. Pre-exponential factors ($k^*_{\infty,i,\mathrm{j}}$) and apparent activation energies ($E_{A,i}$) estimated by means of the minimization of the objective function presented in equation (16) by determining a unique value of apparent activation energy for each reaction.

Catalyst	CO_2 hydrogenation			CO synthesis			Methanol synthesis		
	E_{A,CO_2}	$\ln\left(k^*_{\infty,CO_2,j}\right)$ [a]	R^2	$E_{A,CO}$	$\ln\left(k^*_{\infty,CO,j}\right)$ [a]	R^2	E_{A,CH_3OH}	$\ln\left(k^*_{\infty,CH_3OH,j}\right)$ [a]	R^2
	kJ·mol^{-1}	-	-	kJ·mol^{-1}	-	-	kJ·mol^{-1}	-	-
$In_{40}Ce_{60}$	81.0 ± 0.2	22.77 ± 0.36	0.8861	107.5 ± 0.2	27.68 ± 0.40	0.5169	65.5 ± 0.2	18.82 ± 0.34	0.8251
$In_{60}Ce_{40}$		24.71 ± 0.09	0.9957		29.51 ± 0.08	0.9958		20.81 ± 0.13	0.9871
$In_{80}Ce_{20}$		25.30 ± 0.12	0.9921		30.39 ± 0.26	0.9717		21.24 ± 0.14	0.9854
In_{100}		25.76 ± 0.07	0.9963		30.73 ± 0.07	0.9981		21.74 ± 0.04	0.9986
$In_{80}Zr_{20}$		26.03 ± 0.11	0.9934		31.07 ± 0.10	0.9969		21.92 ± 0.08	0.9939
$In_{60}Zr_{40}$		25.94 ± 0.12	0.9913		30.96 ± 0.08	0.9980		21.81 ± 0.10	0.9904
$In_{40}Zr_{60}$		25.91 ± 0.16	0.9868		31.09 ± 0.15	0.9929		21.65 ± 0.07	0.9954

[a] The unit of the pre-exponential factor ($k^*_{\infty,i,j}$) are $mmol_i \cdot kg_{cat}^{-1} \cdot h^{-1}$.

4 Conclusions

This study has examined the differences between two groups of In_2O_3-based binary oxides catalysts to convert CO_2 and H_2 into methanol. The catalysts were tested in a fixed-bed reactor to evaluate their performances in terms of activity, selectivity and stability. Then, all the samples were analysed with several characterisation techniques to rationalise the experimental results. First of all, the addition of Ce and Zr in the catalysts modifies completely their morphology and textural properties. XRD measurements have suggested the formation of an amorphous In_2O_3-ZrO_2 solid solution for the In_xZr_{100-x} samples, while they have revealed the formation of an In-doped CeO_2 phase in the other group of catalysts, that was also attested by Raman spectroscopy.

Moreover, the adsorption of CO_2 was amplified by the addition of Ce or Zr from 1.8 $mmol_{CO2}\cdot g_{cat}^{-1}$ of the pure In_{100} up to 10.6 $mmol_{CO2}\cdot g_{cat}^{-1}$ of the $In_{40}Ce_{60}$ or 6.6 $mmol_{CO2}\cdot g_{cat}^{-1}$ of the $In_{40}Zr_{60}$; however, this fact results in a different behaviour of the two groups of catalysts. This feature has been ascribed to the higher concentration of oxygen defects and/or vacancies, that have been observed by using XPS and FT-IR measurements and Raman spectroscopy and supported by the literature. In more detail, the results have supported the idea that Zr has an electronic promotion effect on the In_2O_3 by increasing its specific activity. Moreover, the addition of Zr in the catalysts significantly increases the specific surface area and stabilizes the structure of the material, mitigating the effects of sintering. As a result, the deactivation phenomena have been attributed to the loss of specific surface area. On the other hand, the experimental evidence has revealed that In_xCe_{100-x} samples were affected by at least three deactivation mechanisms: sintering of the structure, formation of metallic indium and coking. More specifically, the deactivation rate increases as the amount of Ce rises; besides, the addition of Ce in the catalysts increased their reducibility under reaction condition promoting the reduction of In_2O_3 to metallic indium, that was detected by XRD measurements.

The insights gained from this study may be of assistance to the development of more stable and active catalysts for the CO_2 conversion into methanol. Moreover, the beneficial effect of ZrO_2 could expand the operating condition range for methanol synthesis to develop more efficient processes of one-step processes to produce other added-value products from CO_2 and H_2.

Acknowledgements

The authors would like to acknowledge the Italian regional project SATURNO – Bioeconomy (Piedmont Region 2019-2022, https://saturnobioeconomia.it/) and the project PON Ricerca e Innovazione "REACT-EU" (DM 1062/21) funded by the Italian Ministero dell'Università e della Ricerca (MUR).

References

[1] V. Products, R. Estevez, L. Aguado-deblas, A.A. Romero, D. Luna, F.M. Bautista, J.L. Francisco, A Review on Green Hydrogen Valorization by Heterogeneous, (2022).

[2] W.J. Martinez-Burgos, E. de Souza Candeo, A.B. Pedroni Medeiros, J. Cesar de Carvalho, V. Oliveira de Andrade Tanobe, C.R. Soccol, E.B. Sydney, Hydrogen: Current advances and patented technologies of its renewable production, J Clean Prod. 286 (2021). https://doi.org/10.1016/j.jclepro.2020.124970.

[3] G. Zoppi, G. Pipitone, H. Gruber, G. Weber, A. Reichhold, R. Pirone, S. Bensaid, Aqueous phase reforming of pilot-scale Fischer-Tropsch water effluent for sustainable hydrogen production, Catal Today. 367 (2021) 239–247. https://doi.org/10.1016/J.CATTOD.2020.04.024.

[4] G. Zoppi, G. Pipitone, R. Pirone, S. Bensaid, Aqueous phase reforming process for the valorization of wastewater streams: Application to different industrial scenarios, Catal Today. 387 (2022) 224–236. https://doi.org/10.1016/J.CATTOD.2021.06.002.

[5] P. Runge, C. Sölch, J. Albert, P. Wasserscheid, G. Zöttl, V. Grimm, Economic Comparison of Electric Fuels Produced at Excellent Locations for Renewable Energies: A Scenario for 2035, SSRN Electronic Journal. (2020). https://doi.org/10.2139/ssrn.3623514.

[6] C. Panzone, R. Philippe, A. Chappaz, P. Fongarland, A. Bengaouer, Power-to-Liquid catalytic CO2 valorization into fuels and chemicals: Focus on the Fischer-Tropsch route, Journal of CO2 Utilization. 38 (2020) 314–347. https://doi.org/10.1016/j.jcou.2020.02.009.

[7] E. Alper, O. Yuksel Orhan, CO_2 utilization: Developments in conversion processes, Petroleum. 3 (2017) 109–126. https://doi.org/10.1016/j.petlm.2016.11.003.

[8] S. Brynolf, M. Taljegard, M. Grahn, J. Hansson, Electrofuels for the transport sector: A review of production costs, Renewable and Sustainable Energy Reviews. 81 (2018) 1887–1905. https://doi.org/10.1016/j.rser.2017.05.288.

[9] I. Ganesh, Conversion of carbon dioxide into methanol - A potential liquid fuel: Fundamental challenges and opportunities (a review), Renewable and Sustainable Energy Reviews. 31 (2014) 221–257. https://doi.org/10.1016/j.rser.2013.11.045.

[10] F. Salomone, E. Giglio, D. Ferrero, M. Santarelli, R. Pirone, S. Bensaid, Techno-economic modelling of a Power-to-Gas system based on SOEC electrolysis and CO2 methanation in a RES-based electric grid, Chemical Engineering Journal. 377 (2019) 120233. https://doi.org/10.1016/j.cej.2018.10.170.

[11] E.A. Morosanu, F. Salomone, R. Pirone, S. Bensaid, Insights on a Methanation Catalyst Aging Process: Aging Characterization and Kinetic Study, Catalysts. 10 (2020) 283. https://doi.org/10.3390/catal10030283.

[12] A. Mazza, F. Salomone, F. Arrigo, S. Bensaid, E. Bompard, G. Chicco, Impact of Power-to-Gas on distribution systems with large renewable energy penetration, Energy Conversion and Management: X. 7 (2020) 100053. https://doi.org/10.1016/j.ecmx.2020.100053.

[13] P. Gao, S. Dang, S. Li, X. Bu, Z. Liu, M. Qiu, C. Yang, H. Wang, L. Zhong, Y. Han, Q. Liu, W. Wei, Y. Sun, Direct Production of Lower Olefins from CO 2 Conversion via Bifunctional Catalysis, ACS Catal. 8 (2018) 571–578. https://doi.org/10.1021/acscatal.7b02649.

[14] P. Gao, S. Li, X. Bu, S. Dang, Z. Liu, H. Wang, L. Zhong, M. Qiu, C. Yang, J. Cai, W. Wei, Y. Sun, Direct conversion of CO2 into liquid fuels with high selectivity over a bifunctional catalyst, Nat Chem. 9 (2017) 1019–1024. https://doi.org/10.1038/nchem.2794.

[15] A. Álvarez, A. Bansode, A. Urakawa, A. v. Bavykina, T.A. Wezendonk, M. Makkee, J. Gascon, F. Kapteijn, Challenges in the Greener Production of Formates/Formic Acid, Methanol, and DME by

Heterogeneously Catalyzed CO 2 Hydrogenation Processes, Chem Rev. 117 (2017) 9804–9838. https://doi.org/10.1021/acs.chemrev.6b00816.

[16] H. Guzmán, F. Salomone, E. Batuecas, T. Tommasi, N. Russo, S. Bensaid, S. Hernández, How to make sustainable CO_2 conversion to Methanol: Thermocatalytic versus electrocatalytic technology, Chemical Engineering Journal. (2020) 127973. https://doi.org/10.1016/j.cej.2020.127973.

[17] F. Salomone, G. Bonura, F. Frusteri, M. Castellino, M. Fontana, A.M. Chiodoni, N. Russo, R. Pirone, S. Bensaid, Physico-Chemical Modifications Affecting the Activity and Stability of Cu-Based Hybrid Catalysts during the Direct Hydrogenation of Carbon Dioxide into Dimethyl-Ether, Materials. 15 (2022) 7774. https://doi.org/10.3390/ma15217774.

[18] M. Rivarolo, D. Bellotti, L. Magistri, A.F. Massardo, Feasibility study of methanol production from different renewable sources and thermo-economic analysis, Int J Hydrogen Energy. 41 (2016) 2105–2116. https://doi.org/10.1016/j.ijhydene.2015.12.128.

[19] D. Bellotti, M. Rivarolo, L. Magistri, Economic feasibility of methanol synthesis as a method for CO2 reduction and energy storage, Energy Procedia. 158 (2019) 4721–4728. https://doi.org/10.1016/j.egypro.2019.01.730.

[20] M. Matzen, M. Alhajji, Y. Demirel, Technoeconomics and Sustainability of Renewable Methanol and Ammonia Productions Using Wind Power-based Hydrogen, Journal of Advanced Chemical Engineering. 5 (2015). https://doi.org/10.4172/2090-4568.1000128.

[21] N. Von Der Assen, J. Jung, A. Bardow, Life-cycle assessment of carbon dioxide capture and utilization: Avoiding the pitfalls, Energy Environ Sci. 6 (2013) 2721–2734. https://doi.org/10.1039/c3ee41151f.

[22] F. Arena, K. Barbera, G. Italiano, G. Bonura, L. Spadaro, F. Frusteri, Synthesis, characterization and activity pattern of Cu-ZnO/ZrO2catalysts in the hydrogenation of carbon dioxide to methanol, J Catal. 249 (2007) 185–194. https://doi.org/10.1016/j.jcat.2007.04.003.

[23] G. Bonura, C. Cannilla, L. Frusteri, A. Mezzapica, F. Frusteri, DME production by CO2 hydrogenation: Key factors affecting the behaviour of CuZnZr/ferrierite catalysts, Catal Today. 281 (2017) 337–344. https://doi.org/10.1016/j.cattod.2016.05.057.

[24] F. Frusteri, M. Migliori, C. Cannilla, L. Frusteri, E. Catizzone, A. Aloise, G. Giordano, G. Bonura, Direct CO 2 -to-DME hydrogenation reaction: New evidences of a superior behaviour of FER-based hybrid systems to obtain high DME yield, Journal of CO2 Utilization. 18 (2017) 353–361. https://doi.org/10.1016/j.jcou.2017.01.030.

[25] M.S. Frei, C. Mondelli, R. García-Muelas, K.S. Kley, B. Puértolas, N. López, O. V. Safonova, J.A. Stewart, D. Curulla Ferré, J. Pérez-Ramírez, Atomic-scale engineering of indium oxide promotion by palladium for methanol production via CO2 hydrogenation, Nat Commun. 10 (2019) 3377. https://doi.org/10.1038/s41467-019-11349-9.

[26] O. Martin, A.J. Martín, C. Mondelli, S. Mitchell, T.F. Segawa, R. Hauert, C. Drouilly, D. Curulla-Ferré, J. Pérez-Ramírez, Indium Oxide as a Superior Catalyst for Methanol Synthesis by CO 2 Hydrogenation, Angewandte Chemie International Edition. 55 (2016) 6261–6265. https://doi.org/10.1002/anie.201600943.

[27] M.S. Frei, C. Mondelli, A. Cesarini, F. Krumeich, R. Hauert, J.A. Stewart, D. Curulla Ferré, J. Pérez-Ramírez, Role of Zirconia in Indium Oxide-Catalyzed CO 2 Hydrogenation to Methanol, ACS Catal. 10 (2020) 1133–1145. https://doi.org/10.1021/acscatal.9b03305.

[28] J. Graciani, K. Mudiyanselage, F. Xu, A.E. Baber, J. Evans, S.D. Senanayake, D.J. Stacchiola, P. Liu, J. Hrbek, J.F. Sanz, J.A. Rodriguez, Highly active copper-ceria and copper-ceria-titania catalysts for methanol synthesis from CO2, Science (1979). 345 (2014) 546–550. https://doi.org/10.1126/science.1253057.

[29] E. Sartoretti, C. Novara, F. Giorgis, M. Piumetti, S. Bensaid, N. Russo, D. Fino, In situ Raman analyses of the soot oxidation reaction over nanostructured ceria-based catalysts, Sci Rep. 9 (2019) 3875. https://doi.org/10.1038/s41598-019-39105-5.

[30] E. Sartoretti, C. Novara, A. Chiodoni, F. Giorgis, M. Piumetti, S. Bensaid, N. Russo, D. Fino, Nanostructured ceria-based catalysts doped with La and Nd: How acid-base sites and redox properties determine the oxidation mechanisms, Catal Today. 390–391 (2022) 117–134. https://doi.org/10.1016/j.cattod.2021.11.040.

[31] G. Bonura, M. Cordaro, C. Cannilla, F. Arena, F. Frusteri, The changing nature of the active site of Cu-Zn-Zr catalysts for the CO2 hydrogenation reaction to methanol, Appl Catal B. 152–153 (2014) 152–161. https://doi.org/10.1016/j.apcatb.2014.01.035.

[32] Q. Sun, Y.-L. Zhang, H.-Y. Chen, J.-F. Deng, D. Wu, S.-Y. Chen, A Novel Process for the Preparation of Cu/ZnO and Cu/ZnO/Al2O3 Ultrafine Catalyst: Structure, Surface Properties, and Activity for Methanol Synthesis from CO2 + H2, 1997. https://ac.els-cdn.com/S0021951797915542/1-s2.0-S0021951797915542-main.pdf?_tid=99e7df41-4812-4be0-81ab-e35c0d186efb&acdnat=1541001633_d5baaeeda8daed8868273c094f00e434 (accessed October 31, 2018).

[33] W.-L. Dai, Q. Sun, J.-F. Deng, D. Wu, Y.-H. Sun, XPS studies of Cu/ZnO/Al2O3 ultra-fine catalysts derived by a novel gel oxalate co-precipitation for methanol synthesis by CO2+H2, Appl Surf Sci. 177 (2001) 172–179. https://doi.org/10.1016/S0169-4332(01)00229-X.

[34] I. Langmuir, THE ADSORPTION OF GASES ON PLANE SURFACES OF GLASS, MICA AND PLATINUM., J Am Chem Soc. 40 (1918) 1361–1403. https://doi.org/10.1021/ja02242a004.

[35] S. Brunauer, P.H. Emmett, E. Teller, Adsorption of Gases in Multimolecular Layers, J Am Chem Soc. 60 (1938) 309–319. https://doi.org/10.1021/ja01269a023.

[36] E.P. Barrett, L.G. Joyner, P.P. Halenda, The Determination of Pore Volume and Area Distributions in Porous Substances. I. Computations from Nitrogen Isotherms, J Am Chem Soc. 73 (1951) 373–380. https://doi.org/10.1021/ja01145a126.

[37] A.L. Patterson, The Scherrer Formula for X-Ray Particle Size Determination, Physical Review. 56 (1939) 978–982. https://doi.org/10.1103/PhysRev.56.978.

[38] D. Nath, F. Singh, R. Das, X-ray diffraction analysis by Williamson-Hall, Halder-Wagner and size-strain plot methods of CdSe nanoparticles- a comparative study, Mater Chem Phys. 239 (2020) 122021. https://doi.org/10.1016/j.matchemphys.2019.122021.

[39] V. Mote, Y. Purushotham, B. Dole, Williamson-Hall analysis in estimation of lattice strain in nanometer-sized ZnO particles, Journal of Theoretical and Applied Physics. 6 (2012) 6. https://doi.org/10.1186/2251-7235-6-6.

[40] X. Beaudoux, M. Virot, T. Chave, G. Durand, G. Leturcq, S.I. Nikitenko, Vitamin C boosts ceria-based catalyst recycling, Green Chemistry. 18 (2016) 3656–3668. https://doi.org/10.1039/C6GC00434B.

[41] E. Sartoretti, C. Novara, M. Fontana, F. Giorgis, M. Piumetti, S. Bensaid, N. Russo, D. Fino, New insights on the defect sites evolution during CO oxidation over doped ceria nanocatalysts probed by in situ Raman spectroscopy, Appl Catal A Gen. 596 (2020) 117517. https://doi.org/10.1016/j.apcata.2020.117517.

[42] O. Levenspiel, Chemical Reaction Engineering, 3rd ed., John Wiley & Sons, Inc., 1999. https://pubs.acs.org/doi/10.1021/ie990488g.

[43] R.D. Shannon, Revised Effective Ionic Radii and Systematic Studies of Interatomie Distances in Halides and Chaleogenides, Acta Crystallographica Section A. 32 (1976) 751–767.

[44] D. Liu, W. Lei, S. Qin, L. Hou, Z. Liu, Q. Cui, Y. Chen, Large-scale synthesis of hexagonal corundum-type In2O3 by ball milling with enhanced lithium storage capabilities, J Mater Chem A Mater. 1 (2013) 5274. https://doi.org/10.1039/c3ta00182b.

[45] J. Gan, X. Lu, J. Wu, S. Xie, T. Zhai, M. Yu, Z. Zhang, Y. Mao, S.C.I. Wang, Y. Shen, Y. Tong, Oxygen vacancies promoting photoelectrochemical performance of In2O3 nanocubes, Sci Rep. 3 (2013) 1021. https://doi.org/10.1038/srep01021.

[46] J.Y.Y. Loh, N.P. Kherani, X-ray photospectroscopy and electronic studies of reactor parameters on photocatalytic hydrogenation of carbon dioxide by defect-laden indium oxide hydroxide nanorods, Molecules. 24 (2019) 1–11. https://doi.org/10.3390/molecules24213818.

[47] N. Liu, K. Moumanis, S. Blais, J.J. Dubowski, XPS study of InP/InGaAs/InGaAsP microstructures irradiated with ArF laser in air and deionized water, Synthesis and Photonics of Nanoscale Materials IX. 8245 (2012) 82450E. https://doi.org/10.1117/12.913082.

[48] A. Galtayries, R. Sporken, J. Riga, G. Blanchard, R. Caudano, XPS comparative study of ceria/zirconia mixed oxides: Powders and thin film characterisation, J Electron Spectros Relat Phenomena. 88–91 (1998) 951–956. https://doi.org/10.1016/s0368-2048(97)00134-5.

[49] Z. Wang, A. Pakoulev, Y. Pang, D.D. Dlott, Vibrational Substructure in the OH Stretching Transition of Water and HOD, J Phys Chem A. 108 (2004) 9054–9063. https://doi.org/10.1021/jp048545t.

[50] M. Daturi, C. Binet, S. Bernal, J.A. Pérez Omil, J.C. Lavalley, FTIR study of defects produced in ZrO2 samples by thermal treatmet: Residual species into cavities and surface defects, Journal of the Chemical Society - Faraday Transactions. 94 (1998) 1143–1147. https://doi.org/10.1039/a708208h.

[51] N.C.S. Selvam, A. Manikandan, L.J. Kennedy, J.J. Vijaya, Comparative investigation of zirconium oxide (ZrO2) nano and microstructures for structural, optical and photocatalytic properties, J Colloid Interface Sci. 389 (2013) 91–98. https://doi.org/10.1016/j.jcis.2012.09.014.

[52] N.C. Horti, M.D. Kamatagi, S.K. Nataraj, M.N. Wari, S.R. Inamdar, Structural and optical properties of zirconium oxide (ZrO 2) nanoparticles: effect of calcination temperature, Nano Express. 1 (2020) 010022. https://doi.org/10.1088/2632-959X/ab8684.

[53] R. Dwivedi, A. Maurya, A. Verma, R. Prasad, K.S. Bartwal, Microwave assisted sol–gel synthesis of tetragonal zirconia nanoparticles, J Alloys Compd. 509 (2011) 6848–6851. https://doi.org/10.1016/j.jallcom.2011.03.138.

[54] M.S. Frei, M. Capdevila-Cortada, R. García-Muelas, C. Mondelli, N. López, J.A. Stewart, D. Curulla Ferré, J. Pérez-Ramírez, Mechanism and microkinetics of methanol synthesis via CO2 hydrogenation on indium oxide, J Catal. 361 (2018) 313–321. https://doi.org/10.1016/j.jcat.2018.03.014.